This manuscript is under review for publication in the Canadian Journal of Earth Sciences Special Issue "*Geophysical studies of the lithosphere and plate boundaries*, in honour of Roy Hyndman (October 29, 2024). Constructive feedback is welcome.

Carbonated Mantle Lithosphere from the Western Canadian Cordillera

Nils Peterson[1,3]
Natasha Barrett[2]
and
James K. Russell[3]

Canadian Journal of Earth Sciences

[October 29, 2024]

[1] Galore Creek Mining Corporation, Vancouver, BC Canada.
[2]Mineral Deposits Research Unit, Earth Ocean & Atmospheric Science, University of British Columbia, Vancouver, BC Canada.
[3]Volcanology & Petrology Laboratory, Earth Ocean & Atmospheric Science, University of British Columbia, Vancouver, BC Canada.

*Corresponding Author:
J.K. Russell (krussell@eoas.ubc.ca)

ABSTRACT

Carbonated mantle is widely considered a significant source for many alkaline magmas, yet carbonate minerals are rarely preserved in mantle samples due to their tendency to volatilize under typical magmatic and surface conditions. Here, we report the first occurrence of mantle-equilibrated ("primary") carbonate within spinel peridotite xenoliths from the Pacific Coast Ranges in North America. The xenoliths are hosted in a 19 Ma basanite dyke near the boundary between the Intermontane and Coast Belts of the Canadian Cordillera (Mt. Preston, British Columbia). Magnesian calcite (Ca ratio ~0.90) occurs in all samples as: i) intergranular grains in textural equilibrium with surrounding minerals (granoblastic texture, ≤ 0.4 mm grains; < 2 vol%), ii) inclusions within mantle silicates; and as iii) intergranular or fracture-filling veins. Sulphides (pentlandite and chalcopyrite), also occur in equilibrium with the carbonate. Geothermometry on carbonate-bearing mantle xenoliths record paleo-equilibrium temperatures of ~815 to 1120 °C, corresponding to depths of ~32 to 55 km on a model geotherm for warm, thin Cordilleran-style lithosphere. Bulk-rock C–O isotopes of the xenolith suite vary as $\delta^{13}C$ = -3 to -6, and $\delta^{18}O$ = 10 to 12. Collectively, the textural, geochemical and isotopic evidence suggest that a carbonate melt with associated monosulphide solution metasomatized and enriched previously depleted mantle lithosphere. The metasomatic fluids sourced from the subduction of oceanic crust beneath North America during Coast Plutonic Belt magmatism when Mt. Preston was in an arc to back arc position. The host basanite dyke contains magmatic groundmass calcite ($\delta^{18}O$ = 14±, $\delta^{13}C$ = -4±, $^{87}Sr/^{86}Sr$ = 0.7040±) indicating a high intrinsic P_{CO2} that inhibited thermal decomposition of mantle carbonate within the xenoliths during ascent.

Keywords: Mantle-lithosphere, xenolith, dyke, peridotite, carbonate, sulphide, basanite, Canadian-Cordillera, British Columbia.

1. Introduction

Mantle-derived xenoliths are commonly sampled and transported to the surface in mafic magmas and represent direct samples of the Earth's lithospheric mantle (Pearson et al., 2003; Russell and Jones, 2023 and references therein). Beneath mobile belts such as the Canadian Cordillera the mantle lithosphere is relatively thin (<35 km) and warm (800–1200 °C; Hyndman et al., 2017 and references therein) and dominated by spinel peridotite. In addition to the major mineral phases, the mantle lithosphere can host accessory minerals including amphiboles (e.g., Ghent et al., 2019), apatite, phlogopite (e.g., Canil and Scarfe, 1989), sulphides (e.g., Delpech et al., 2012; Rielli et al., 2022), and carbonates (Yaxley et al., 1991; Ionov et al., 1996; Rudnick et al., 1993; Ducea et al., 2005). These accessory phases can be important indicators of past metasomatic events (i.e., pervasive fluid or melt enrichment) that influence the mantle solidus, and hence, control mantle melting (e.g., Francis and Ludden, 1995; Laurora et al., 2001). Such phases have also been used to estimate mantle volatile budgets and to inform on the transport and mobilization of metals within the mantle lithosphere (e.g., Rielli et al., 2022).

Primary (i.e. mantle-equilibrated) carbonate is stable under typical upper mantle redox conditions, however, is rarely preserved due to rapid decarbonation during xenolith entrainment and transport of carbonated peridotite (e.g., Canil, 1990). Nevertheless, primary carbonate has been reported for mantle xenolith suites deriving from a variety of tectonic settings including active or paleo-subduction zones (e.g., Laurora et al., 2001; Demény et al., 2004; Ducea et al., 2005), intraplate settings (e.g., Moine et al., 2004) and rift margins (e.g. Lee et al., 2000; Perkins et al., 2006). Most primary carbonates are considered to result from enrichment events shortly before eruption, due to textural/chemical disequilibrium (e.g., Lee et al., 2000; Demény et al., 2004; Moine et al., 2004; Ducea et al., 2005; Ionov et al., 2006). In some instances, primary carbonate preserved in mantle xenoliths has been interpreted as chemically and isotopically equilibrated with the mantle (e.g., Ionov et al., 1996; Yaxley et al., 1998), although the original textures are typically destroyed by subsequent melting of the carbonate phases during transport to be replaced by quenched glass.

Here, we report on a new suite of lithospheric mantle xenoliths preserved in a mafic dyke exposed at Mt. Preston in western British Columbia (BC; Fig. 1) and described by

Peterson et al. (2006) and Peterson (2010). This occurrence is distinguished, relative to others in the Canadian Cordillera, because it is located at the westernmost margin of the Intermontane Belt, close to the Coast Belt margin (e.g., Wheeler et al., 1991; Fig. 1). These mantle xenoliths, therefore, inform on the thermal and compositional state of the mantle lithosphere underlying this under-represented portion of the Canadian Cordillera. Furthermore, these xenoliths are unique because they preserve mantle-equilibrated (i.e. primary) carbonate in textural and chemical equilibrium. The suite of peridotite xenoliths provides direct evidence for, and the origins of, carbonate-melt metasomatism of the mantle lithosphere underlying this region of the Canadian Cordillera.

2. Geological Setting

2.1. Tectonic Framework

The Canadian Cordillera is an amalgamation of terranes accreted onto the North American margin from the mid- to early Jurassic (~185 Ma) to the Late Cretaceous (90 to 85 Ma, Insular Belt rocks) (Monger et al., 1982; Gehrels et al., 2009). The terranes comprising the Intermontane Belt have been interpreted as related fragments of a late Paleozoic to early Mesozoic island arc (Stikine and Quesnel terranes), and its associated accretionary complex (Cache Creek terrane). The Intermontane Belt is separated from the Insular Belt to the west by the Coast Belt, comprising the Coast Mountains Batholith (or Coast Plutonic Complex), the roots of a Middle Jurassic to Eocene magmatic arc (van der Heyden, 1992; Monger et al., 1994; Gehrels et al., 2009), and related rocks (Fig. 1).

Mafic volcanic centers are ubiquitous in the Canadian Cordillera, and they commonly sample the lithosphere underlying their eruptive localities (e.g., Edwards and Russell, 2000; Canil and Hyndman 2023; and references therein). These occurrences have supported numerous studies of the Cordillera's mantle lithosphere (e.g., Canil and Scarfe, 1989; Peslier et al., 2000; Peslier et al., 2002; Harder and Russell, 2006; Francis et al., 2010 and references therein). Most evidence for metasomatic events within the mantle lithosphere underlying the Canadian Cordillera is indirect (i.e. cryptic metasomatism) and based on geochemical compositions of peridotite xenoliths (e.g., Francis and Ludden, 1995; Peslier et al., 2002). Rare direct evidence for mantle metasomatic events within the Cordilleran mantle derives

from the presence of accessory phlogopite (Canil and Scarfe, 1989) or pargasitic amphibole (Ghent et al., 2019) within peridotite xenoliths.

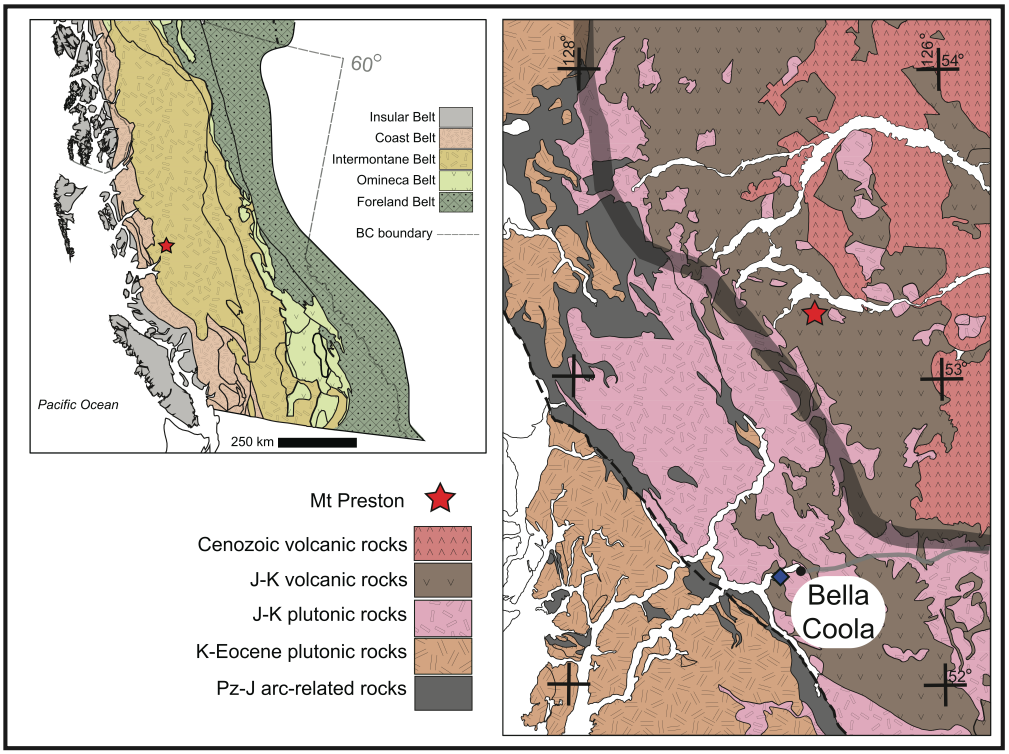

Fig. 1. Location of the Mt. Preston mantle xenolith locality within the Canadian Cordillera. (A) Mt. Preston field site (red star) shown in the context of the major tectono-morphologic belts of the Canadian Cordillera (modified from Wheeler et al., 1991). (B) Regional geology of the Mt. Preston field site (red star) is situated south of Eutsuk Lake, approximately 40 km east of the Coast Belt. Thick, grey-shaded line indicates Intermontane Belt–Coast Belt boundary.

2.2. Host Dyke

A xenolith-bearing dyke outcrops on a ridge ~3 km southeast of Mt. Preston at 53° 13' 3" N, 126° 41' 56" W (Fig. 1). The dyke is exposed at the ridge crestline and can be traced continuously down a steep south-facing slope for ~110 m (Fig. 2) and several hundred metres further on an inaccessible vertical face. Contacts with the wall rocks are sharply defined and the dyke varies in thickness, from ~1 to 2 m, where both contacts are visible.

The dyke is aphyric, holocrystalline, moderately vesicular (5–30%) and features an aphanitic groundmass (Fig. 2). The groundmass mineralogy comprises ~40 vol.% plagioclase, ~25 % olivine (≤0.5 mm), ~35 % clinopyroxene (≤0.2 mm), and ~3 % of ≤ 0.1 mm subhedral to anhedral crystals of ulvöspinel. Magmatic carbonate, identified as near end-member

calcite, occurs as ≤0.5 mm laths and patches in the groundmass, and as larger subhedral grains (≤1 mm) filling or lining vesicles (Fig. 2D–E). Other minor phases include alkali feldspar, nepheline, and apatite.

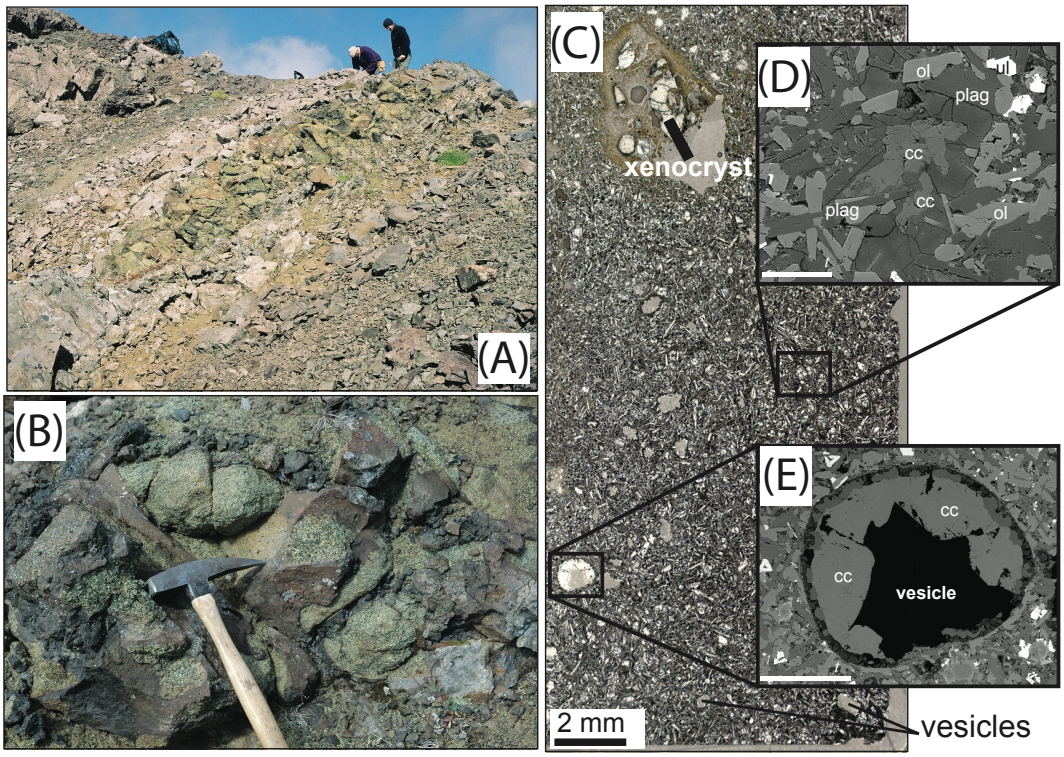

Fig. 2. Mt. Preston mantle xenolith field locality within basanite dyke. (A) Field photograph showing distribution of mantle xenoliths in the dyke. (B) Detailed view of closely packed mantle xenoliths within the dyke and separated by small volume of basanite melt. (C) Photomicrograph in plane-polarized light (PPL) of basanite showing fresh, unaltered, groundmass mineralogy and volcanic texture. The basanite is aphyric, micro-vesicular and contains a partially digested mantle-derived xenocryst. (D) Scanning electron microscope (SEM) images illustrating primary groundmass mineralogy, and their textural relationships, including olivine, plagioclase, ulvöspinel (ul), and calcite (cc). (E) SEM image of vesicle containing calcite (cc).

Major element compositions and their trace and rare earth element contents are reported in Supplementary materials (Table SM1). Chemically the dyke is a basanite, has an SiO_2 content of ~43 wt.%, an Mg# of 62, and contains 5 wt.% normative nepheline. The basanite has a calculated liquidus of ~1250–1300 °C (MELTS modeling; 15 kbar, QFM, 0–1 wt.% H_2O; Asimow and Ghiorso, 1998). A single sample of the dyke was dated by $^{40}Ar/^{39}Ar$ methods and returned a plateau age of 18.72 ± 0.26 Ma (± 2s) representing a Neogene (early Miocene) crystallization age (see Supplementary Material SM2).

157 2.3. Xenolith Occurrence

158 Mantle-derived peridotitic xenoliths are especially abundant in the outcroppings
159 situated 4–8 m below the ridge crest where the dyke narrows to ~1 m in width (Fig. 2A, B).
160 At this location, the xenoliths constitute 50–80 % of the dyke and are concentrated enough
161 to be locally clast-supported (Fig. 2B). The mean diameter of xenoliths at this locality is ~15
162 cm and the largest xenolith measured was ~40–50 cm in diameter. Over 150 xenoliths were
163 collected from Mt. Preston and a representative group of 51 xenoliths studied in detail. The
164 peridotite xenoliths are dominated by lherzolite, well-preserved, and show no signs of
165 reacting with the host magma even though several peridotite blocks are crosscut by one or
166 more thin (1–5 mm) planar veins of melt. Xenolith angularity crudely correlates inversely
167 with size.

168 2.4. Dyke Wall Rock

169 The Mt. Preston region is underlain by Early to Middle Jurassic volcaniclastic rocks
170 of the Hazelton Group, comprising metamorphosed volcanic to volcanoclastic and mudstone-
171 dominated sedimentary rocks (Gordee et al., 2005; Mahoney et al., 2005). In the area of the
172 dyke of interest, only volcaniclastics (trachyandesite to dacite, by major element chemistry)
173 are present. In the region, Hazelton rocks are intruded by post-ca. 136 Ma, metamorphosed
174 mafic to intermediate dykes (Gordee et al., 2005); one of these dykes, a narrow (<1 m width)
175 trachybasalt located within 10 m of the xenolith-bearing dyke of interest, was sampled and
176 dated ($^{40}Ar/^{39}Ar$) as 87.74 ± 0.71 Ma (± 2s). There are no carbonate-rich lithologies noted or
177 previously mapped in the region of Mt. Preston.
178

179 **3. METHODS**

180 3.1. Bulk Geochemistry

181 For bulk geochemical analysis samples were prepared at the UBC Department of
182 Earth and Ocean Sciences, by jaw crusher and pulverized in a tungsten carbide ring mill, then
183 sieved to a grain size of <0.42mm. Analysis of powders for major and trace elements, ferrous
184 iron, H_2O, and CO_2 was carried out at the Geochemical Laboratories, McGill University,
185 Montreal. Major elements were analyzed by X-ray fluorescence (XRF) on fused beads from

ignited samples; trace elements were analyzed for using pressed powder pellets. XRF analysis was done on a Philips PW2440 spectrometer. Total iron was determined by XRF, and FeO content was determined by volumetric analysis (ammonium metavanadate titration). Samples were analyzed for CO_2 on an ELTRA CS-800 carbon/sulphur infrared (IR) analyzer. H_2O+ (structurally bonded water) was determined by difference using loss on ignition (LOI), CO_2, SO_3, halogens, and FeO analyses.

3.2. Mineral Compositions

Compositions of minerals were measured on a fully automated CAMECA SX-50 electron microprobe at the University of British Columbia, Department of Earth and Ocean Sciences. Operating conditions in wavelength-dispersion mode included: excitation voltage of 15 kV, beam current of 20 nA, 20 s peak count time, 10 s background count time, and a beam diameter of 5 μm. For carbonate a beam current of 10 nA and a spot diameter of 10 μm was used. Data reduction was completed using the 'PAP' $\phi(\rho Z)$ method (Pouchou and Pichoir, 1985). Criteria for exclusion of analysis points included low or high totals (<98 or >102 %) or poor totals of oxygen relative to the cation sums. The cations sum was set to 4 for pyroxenes, 3 for olivine and spinel. Analyses were excluded if the oxygen sum was <5.95 or >6 for pyroxenes, <3.95 or >4 for olivine and spinel. For geothermometry purposes, in each xenolith at least 8 coexisting clinopyroxene and orthopyroxene grains were analyzed. These analyses were made for each phase adjacent to shared grain boundaries (~20 μm from grain edges); no zoning was observed in these phases.

3.3. Stable Isotopes

Oxygen, carbon, and strontium isotopic analyses on carbonates were performed on leachates of bulk-rock powders (like other mantle-derived carbonate studies, e.g. Ionov et al. 1993), and in the case of dyke and country rock, also from tungsten carbide microdrilling of carbonate-rich patches. All powdered samples were analyzed at the PCIGR, University of British Columbia, in a Finnigan Delta XL Plus mass spectrometer, using a gas bench with A200 S autosampler.

Oxygen and strontium isotopic compositions of the silicate fraction of the basanite dyke were determined after removal of carbonate from the bulk-rock powders. Powders were immersed in 10% hydrochloric acid, agitated in an ultrasonic bath for 10 minutes, then

separated from the leachate via centrifuge. The leaching process was verified by X-ray diffraction. Sample analysis was performed at the Facility for Isotope Research at Queen's University, Kingston, Ontario. Analysis followed the BrF5 method of Clinton and Mayeda (1963), on a Finnegan MAT 252 mass spectrometer.

4. Xenolith Petrography

4.1. Peridotite Xenoliths

Of the 51 xenoliths studied in detail, 48 have a typical assemblage of olivine (ol), clinopyroxene (cpx), orthopyroxene (opx) and spinel (spl). Two websterites lacking olivine and containing spinel and plagioclase (NP-MP05-69, -96), and a dunite lacking orthopyroxene (NP-MP05-150) were also described. Dunites are a minor but common component in Cordilleran suites. According to the definition of Shi et al. (1998), the Mt. Preston suite is unimodal (i.e., lherzolite-dominated) and, in that regard, like most other xenolith suites in the Canadian Cordillera; bimodal suites (i.e., enriched in harzburgite) are found in northwestern BC and southern Yukon (Shi et al., 1998; Francis et al., 2010).

Individual xenoliths exhibit granular textures and substantial medium grain size variations (~0.5–2 mm), but rarely contain megacrysts (outsized grains). About a third of the xenoliths show weak to moderate planar fabrics (i.e., mineralogical banding and mineral foliation) at the hand-sample scale. Foliation tends to be stronger (or more easily observed) in fine-grained samples and is weaker in samples with increasing median grain size. Banding is observed as 1–3 mm wide bands of spinel, repeating on a 1 cm scale, or 2–3 mm wide indistinct bands of clinopyroxene, repeating on an approximately 1–2 cm scale. Larger scale segregations, or possibly bands of olivine and clinopyroxene (~1 cm width or greater) also occur.

4.2. Carbonate Petrography

We investigated the presence of accessory carbonate in mantle xenoliths using a Cambridge Image Technology™ CL8200 Mk4 cold cathodoluminescence (CL) system attached to a petrographic microscope at the University of British Columbia. Operating conditions included an excitation voltage of 15 kV and a current of 350 μA. Granular

carbonate (intergranular or inclusions; Fig. 3A) and/or carbonate veins are found as an accessory phase in all mantle xenoliths and are commonly associated with pentlandite and chalcopyrite (Fig. 3). A single rutile grain was found included in one calcite grain. No hydrous minerals, nor interstitial glass indicative of disequilibrium, were observed. We also used CL to test for the presence of carbonate in two additional crustal xenoliths from the same dyke and mantle xenoliths from two other localities in the Canadian Cordillera. CL examination of these samples found no carbonate.

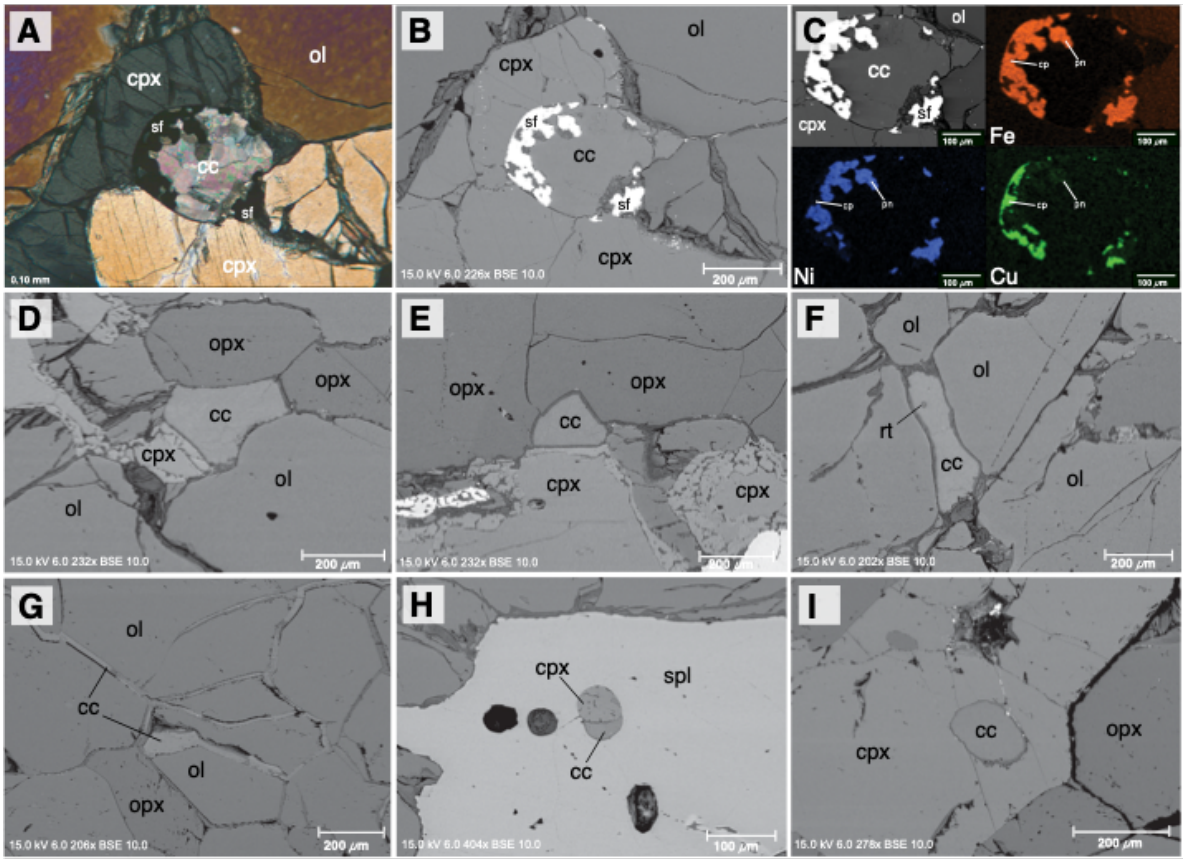

Fig. 3. Cross-polarized (XPL) and backscattered electron (BSE) images showing the three carbonate (cc) habits found in Mt. Preston mantle xenoliths. (A–C) show carbonate (calcite) in association with sulphides (cpy: chalcopyrite and pn: pentlandite), with Fe, Ni, and Cu EPMA element maps shown in panel C. (D–E) show intergranular carbonate with olivine (ol), orthopyroxene (opx), and clinopyroxene (cpx). (G–I) show carbonate as an interstitial phase (G) or as inclusions in association with cpx (panels H and I).

The xenolith-hosted intergranular carbonate (Mg-bearing calcite; X_{Ca} of 86–94) is found as discrete ≤0.4 mm grains exhibiting uniform extinction, or as patches with distinct internal crystallographic subdomains (Fig. 3A). Texturally the intergranular carbonate

appears to be in equilibrium with coexisting silicate phases, as suggested by shared triple-point grain boundaries (Fig. 3A–F). Some intergranular carbonate shows concentric zones of Mg-enrichment. Carbonate also occurs as ≤0.2 mm inclusions (Fig. 3H & 3I) in other mantle minerals. Carbonate veins (≤0.1 mm wide) appear as intergranular and crosscutting features (Fig. 3G); some carbonate veins merge with larger grains of carbonate (Fig. 3). Sparse, thin veinlets of basanite crosscut all features including carbonate veins, indicating that the carbonate predates entrainment by the basanite magma and, thus, are a mantle feature.

4.3. Sulphide Petrography

Pentlandite and chalcopyrite (≤0.1 mm) were noted in eight of the xenoliths examined by CL and have modal abundances < 1 %. They occur at the edges of carbonate grains (Fig. 3A–C) in contact with silicates, at the margins of carbonate veins, and in inclusion trails with or without associated carbonate.

5. Geochemistry

5.1. Major and Trace Element Geochemistry

Bulk major element compositions of mantle xenoliths have Mg# of 87 to 91, Al_2O_3 contents of 1.2 to 4.7 wt.% for lherzolites (0.18 wt.% for dunite NP-MP05-160B and 11.9 wt.% for websterite NP-MP05-69) (see Supplementary Material Table SM3). Major element compositions are consistent with other mantle-derived xenolith suites in the Canadian Cordillera (Fig. 4; Shi et al., 1998; Peslier et al., 2002; Harder and Russell, 2006; Francis et al., 2010) and other continental spinel-bearing peridotites worldwide, reflecting varying degrees of melt extraction from a fertile mantle source (Peslier et al., 2002).

Trace and rare earth element (REE) compositions (Fig. 5; Supplementary Material Table SM3) are like other BC mantle suites and show no pronounced single element anomalies. Rare earth element patterns are light rare earth element (LREE; La to Sm) depleted to flat (Fig. 5A–B). Many patterns show a ‘spoon-shaped’ profile of LREE depletion, with slight enrichment of the lightest REEs (e.g., La, Ce); only one pattern (the harzburgite) is weakly LREE enriched relative to the middle (MREE; Eu to Ho) and heavy (HREE; Er to Lu) rare earth elements. The dunite is especially demonstrative of LREE enrichment; the LREE contents are like that of some other xenoliths from the suite, while the MREE and

HREE concentrations are below detection.

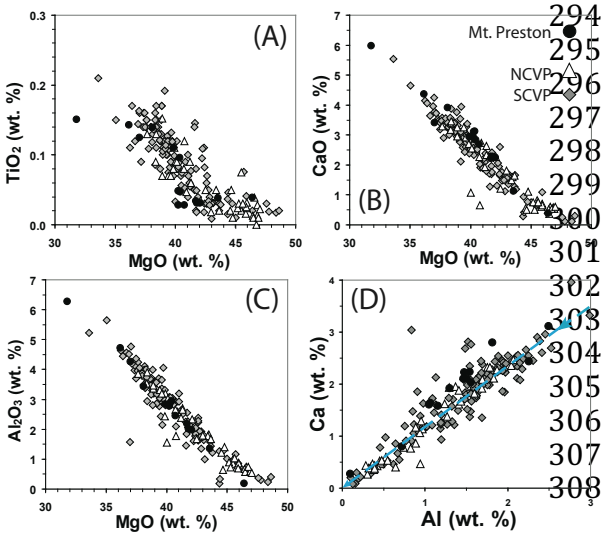

Fig. 4. Bulk-rock major element proxies of melt depletion from the Mt. Preston mantle xenolith suite and published data for Canadian Cordilleran xenoliths. (A–C) Major elements (TiO_2 wt. %, CaO wt. %, and Al_2O_3 wt. %) *vs*. MgO wt. % for mantle xenoliths (lherzolites, harzburgites, and dunites) from Mt. Preston, Northern Cordilleran Volcanic Province (NCVP; see Francis et al., 2010), and Southern Cordilleran Volcanic Province (SCVP; Peslier et al., 2002). (D) Ca *vs*. Al wt. % in mantle xenoliths from the Canadian Cordillera. Data sources as in A–C. Blue dashed line with arrows indicates expected trend for depletion of oceanic peridotite (Boyd, 1989).

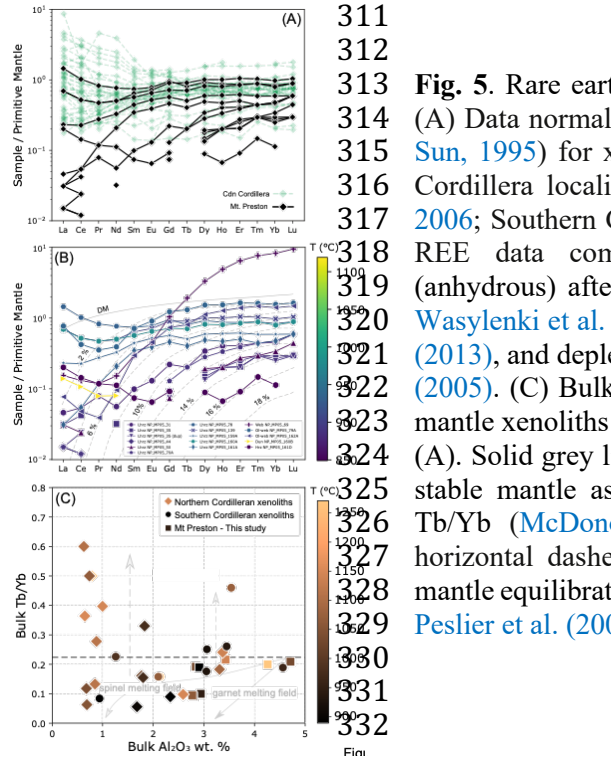

Fig. 5. Rare earth element (REE) contents of mantle xenoliths. (A) Data normalized to primitive mantle (PM; McDonough and Sun, 1995) for xenoliths from Mt. Preston and other Canadian Cordillera localities (Northern Cordillera, Harder and Russell, 2006; Southern Cordillera, Peslier et al., 2002). (B) Mt. Preston REE data compared to REE fractional melting models (anhydrous) after Warren (2016) using the melting reaction of Wasylenki et al. (2003), partition coefficients from Sun & Liang (2013), and depleted mantle (DM) values from Workman & Hart (2005). (C) Bulk-rock Tb/Yb *vs*. Al_2O_3 for Canadian Cordillera mantle xenoliths (after Peslier et al., 2002); data sources are as in (A). Solid grey lines denote melting trends for spinel and garnet stable mantle assemblages (Bodinier et al., 1988). Chondritic Tb/Yb (McDonough and Sun, 1995) is also shown (black horizontal dashed line). Colour bars in (B) and (c) represent mantle equilibration temperatures from Harder & Russell, (2006), Peslier et al. (2002), and this study.

Tb/Yb ratios for peridotites (Fig. 5C) can be indicative of whether melt extraction has occurred in the spinel or garnet stability field, as Yb partitions strongly into garnet as a residual phase, resulting in strong Tb/Yb decreases even at small degrees of melting (Bodinier et al., 1988). The Mt. Preston peridotite compositions are consistent with melt

extraction in the spinel stability field (Fig. 5C), as with other suites in the Cordillera (Peslier et al., 2002). Terbium enrichment has been interpreted as the result of significant metasomatism (Peslier et al., 2002). None of the Mt. Preston xenoliths analyzed show Tb enrichment over Yb relative to chondrite, suggesting that metasomatic processes did not disturb the MREEs or if so, very little. We found no correlation between the degree of melt depletion or metasomatism with the mantle equilibration temperatures (section 5 below) as color coded in Figures 5B and 5C.

Table 1. Radiogenic and stable isotopic data for Mt. Preston (MP-) mantle xenoliths including Sr datasets for carbonate fractions (CF) in bulk rock (WR) powders, equilibration temperatures calculated after Brey and Kohler, (1990), approximate CO_2 contents via loss on ignition (LOI), and bulk rock Al_2O_3 wt. % values (proxy for melt depletion). Values also reported for Sr standards (SRM987) and for replicates[1].

Strontium (± 2σ)

Sample / Description	Rock Type	$^{87}Sr/^{86}Sr$	$^{86}Sr/^{88}Sr$	T (°C)	1σ	wt. % CO_2	Al_2O_3 wt.%
MP05-159A / (CF)	Lherzolite	0.704618 ± 0.000008	0.1198	863	11	0.33	2.84
MP05-160A / (CF)	Lherzolite	0.704432 ± 0.000008	0.1196	919	9	0.33	4.26
MP05-164A / (CF)	Lherzolite	0.704610 ± 0.000008	0.1196	828	8	0.29	2.91
MP05-164A[1] / (CF)	Lherzolite	0.704607 ± 0.000009	0.1199	828	8	0.29	2.91
SRM987 (600 ng)	Standard	0.710220 ± 0.000008	0.1195	–	–	–	–
SRM987 (300 ng)	Standard	0.710233 ± 0.000008	0.1200	–	–	–	–
SRM987 (600 ng)	Standard	0.710232 ± 0.000007	0.1192	–	–	–	–

Carbon and Oxygen (± 1σ)

Sample	Rock Type	$\delta^{13}C$ (‰ vs. VPDB)	$\delta^{18}O$ (‰ vs. VSMOW)	T (°C)	1σ	wt. % CO_2	Al_2O_3 wt.%
MP05-31	Lherzolite	-4.36 ± 0.10	12.46 ± 0.08	842	4	0.33	2.94
MP05-35	Lherzolite	-5.67 ± 0.06	11.20 ± 0.06	862	13	0.33	2.01
MP05-35[1]	Lherzolite	-6.09 ± 0.04	10.92 ± 0.05	862	13	0.33	2.01
MP05-44	Lherzolite	-5.72 ± 0.04	11.17 ± 0.03	858	8	0.33	2.18
MP05-50	Lherzolite	-5.74 ± 0.07	10.91 ± 0.11	811	19	0.26	2.45
MP05-69	Websterite	<d/l	<d/l	867	20	0.11	11.9
MP05-70A	Lherzolite	-4.41 ± 0.06	11.35 ± 0.06	869	9	0.29	2.77
MP05-78	Lherzolite	-6.03 ± 0.03	12.26 ± 0.05	888	9	0.26	3.43
MP05-79A	Ol-Websterite	-4.20 ± 0.05	11.82 ± 0.05	891	12	0.33	6.27
MP05-139	Lherzolite	-5.75 ± 0.07	11.26 ± 0.09	862	6	0.26	4.71
MP05-159A	Lherzolite	-5.79 ± 0.05	12.35 ± 0.05	863	11	0.33	2.84
MP05-160A	Lherzolite	-3.72 ± 0.04	11.41 ± 0.04	919	9	0.33	4.26
MP05-160B	Dunite	-3.37 ± 0.06	11.64 ± 0.07	1044	7	0.29	0.18
MP05-161D	Harzburgite	-3.51 ± 0.08	10.26 ± 0.09	816	19	0.26	1.36
MP05-162A	Ol-Websterite	-4.19 ± 0.05	11.34 ± 0.04	866	7	0.26	5.75
MP05-164A	Lherzolite	-5.87 ± 0.03	11.30 ± 0.06	828	8	0.29	2.91

5.2. Stable isotopes (C–O)

Carbon and oxygen isotope compositions of carbonate from the mantle xenoliths, the host basanite, and the wall rocks are reported in Table 1 and plotted in Figure 6 (see also Supplementary Material Table SM1). Isotopic analyses were performed on leachates of bulk-

rock powders and, in the case of dyke and country rock, also on carbonate recovered by micro-drilling of carbonate-rich phases. The wall rock sample was collected <20 m away from the basanite.

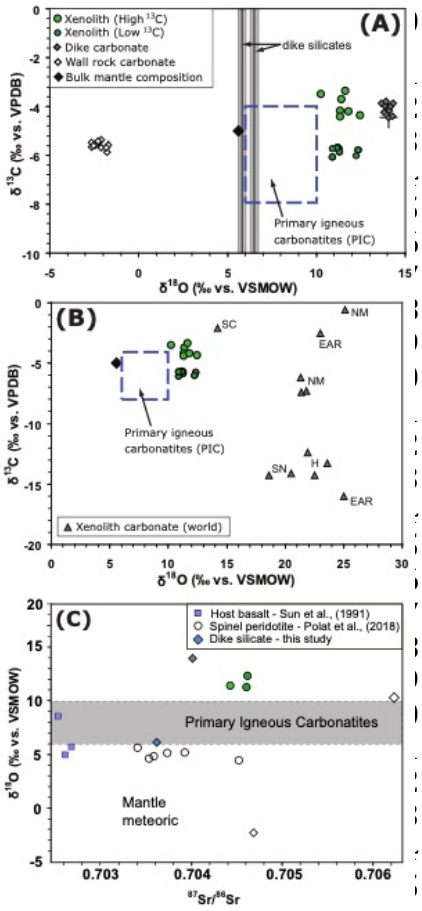

Fig. 6. Carbon and oxygen isotope compositions for carbonates in: (A) Mt. Preston mantle xenoliths, basanite dyke, and wall rock from Mt. Preston, and (B) for worldwide samples of mantle xenolith-hosted carbonate. Xenolith-hosted carbonate, including: NM New Mexico (Perkins et al., 2006); SN Sierra Nevada (Ducea et al., 2005); H Hungary (Demény et al., 2004); SC Slave Craton (van Achterbergh et al., 2002); EAR East African Rift (Lee et al., 2000). Analytical uncertainties are generally smaller than symbols. Primary carbonatite field is from Taylor et al. (1967) and Keller and Hoefs (1995) and bulk mantle value from Harmon and Hoefs (1995) and Deines (2002). (C) Strontium isotope composition of carbonate within mantle peridotites, basanite dyke, and wall rock *vs*. oxygen isotope composition. Also shown are bulk rock Sr data for silicate fractions from the Mt. Preston dyke, peridotite xenoliths (Tasse suite xenoliths, Polat et al., 2018), and sodic and potassic alkaline olivine basanite dykes (Jacques Lake, Big Timothy Mountain, West Kettle River; Sun et al., 1991). Composition range for primary carbonatites (last 500 Ma) from Taylor et al. (1967), Keller and Hoefs (1995), and Barker (1996).

Carbonate recovered from these three sources (mantle xenoliths, dyke, wall rock) have distinct carbon-oxygen isotopic compositions. Dyke carbonate has $\delta^{18}O_{VSMOW}$ compositions of 13.7 to 14.3 ‰, and $\delta^{13}C_{VPDB}$ compositions of -3.8 to -4.5 ‰. In the dyke, $\delta^{18}O_{VSMOW}$ values are ~14 ‰ greater than wall rock, which is 8 ‰ higher than the associated silicates in the dyke, indicating isotopically distinct sources for the carbonate in the dyke and the wall rock (Fig. 6; Table 1). The wall rock carbonate has $\delta^{18}O_{VSMOW}$ compositions of -1.7 to -2.6 ‰, and $\delta^{13}C_{VPDB}$ compositions of -5.4 to -5.9 ‰. The $\delta^{18}O$ composition of wall rock carbonate (~2 ‰ less than VSMOW) is consistent with equilibration with meteoric water. The carbonate within the dyke shows no signs of isotopic exchange with meteoric waters, as isotopic exchange with these fluids would deplete the carbonate in ^{18}O. The isotopic

compositions of the carbonates from the dyke are also consistent with unaltered magmatic carbonate. Additionally, there is no distinction between bulk-rock and micro-drilled analyses, ruling out small-scale isotopic variations from multiple isotopic sources.

Carbonate recovered from fourteen mantle xenoliths plot as two distinct groups based on their ^{13}C compositions. The ^{13}C-enriched group (Fig. 6A) has $\delta^{13}C$ compositions between -3.4 and -4.4 ‰ (VPDB), while the ^{13}C-depleted group (7 xenoliths) has $\delta^{13}C$ compositions between -5.7 and -6.1 ‰ (VPDB). Both groups have similar ranges (10.3 to 12.5 ‰ (VSMOW)) of $\delta^{18}O$. All but two of the mantle xenolith samples used for stable isotope analysis contained both granular carbonate and carbonate veins. The other two contained only vein carbonate and they are part of the ^{13}C-depleted group.

The carbonates from the Mt. Preston mantle xenoliths are closer to primary mantle isotopic compositions than other reported mantle-hosted carbonates (Fig. 6B; Lee et al., 2000; van Achterbergh et al., 2002; Demény et al., 2004; Ducea et al., 2005; Perkins et al., 2006). The Mt. Preston xenoliths host carbonate having $\delta^{18}O$ compositions less than 3 ‰ greater than the field established to date for primary mantle-derived carbonatites (Fig. 6b; Taylor et al., 1967; Keller and Hoefs, 1995). In other studies, authors report enriched $\delta^{18}O$ compositions in mantle-derived carbonate in xenoliths (Lee et al., 2000; van Achterbergh et al., 2002; Demény et al., 2004; Ducea et al., 2005; Perkins et al., 2006) that are interpreted to indicate isotopic disequilibrium between carbonate and host silicates and explained by short durations between enrichment and eruption. The global mantle average for the $\delta^{18}O$ composition of the silicate and oxide phases in spinel peridotite xenoliths is approximately 5-5.7 ‰ relative to VSMOW depending on the phase.

5.3. Radiogenic Isotopes (Sr)

The isotopic signatures of the carbonate source are given by the $^{87}Sr/^{86}Sr$ ratios (Fig. 6C Table 1). The Sr isotopes reveal different source compositions for carbonate in the Mt. Preston dyke (silicate portion: $^{87}Sr/^{86}Sr \sim 0.7040$, carbonate portion: $^{87}Sr/^{86}Sr \sim 0.7036$) *versus* the country rock samples ($^{87}Sr/^{86}Sr \sim 0.7047$). These $^{87}Sr/^{86}Sr$ values from the Mt. Preston dyke are within the upper range of previously reported Canadian Cordilleran (xenolith-hosting) alkaline basalts ($^{87}Sr/^{86}Sr = 0.7024–0.7041$; Polat et al., 2018; Sun et al., 1991). Mantle xenoliths (carbonate fraction) record slightly more radiogenic $^{87}Sr/^{86}Sr$ ratios

(0.7044 to 0.7046) than the Mt. Preston dyke samples ($^{87}Sr/^{86}Sr = 0.7040$). Similar Sr isotopic values were recorded for the Tasse xenolith suite in the southern Canadian Cordillera (Polat et al., 2018; $^{87}Sr/^{86}Sr \sim 0.7041$), however, both the Tasse suite and the Mt. Preston suite are slightly more radiogenic than other average values for xenoliths suites reported within other southern Canadian Cordillera by Sun et al. (1991) (Jacques Lake: $^{87}Sr/^{86}Sr \sim 0.7027$, Big Timothy Mountain: $^{87}Sr/^{86}Sr \sim 0.7030$, West Kettle River: $^{87}Sr/^{86}Sr \sim 0.7033$, Lassie Lake: $^{87}Sr/^{86}Sr \sim 0.7037$).

6. Geothermometry

Mineral chemical compositions of all major phases (clinopyroxene (cpx), orthopyroxene (opx), olivine (ol), and spinel (spl) in 51 xenoliths were measured by electron microprobe, for the purposes of two-pyroxene geothermometry based on the Brey and Köhler (1990) (BK90) calibration. Our approach was to perform thermometry on sequential batches of 5 samples and continue expanding the population until there was no further change in the maximum and minimum temperature (Fig. 7A; see Harder and Russell, 2006). We suggest that the results from 51 samples closely approximate the entire temperature range within the underlying mantle lithosphere.

The Brey and Köhler (1990) geothermometer has a temperature gradient with pressure of ~1.5–1.8 ˚C/Kb. However, we assume that all xenoliths record temperatures along a model geotherm thereby removing the need to adopt an arbitrary pressure for the geothermometric calculations. Operationally we do this by solving the BK90 equation simultaneously with the equation for the model geotherm (see below). The geothermometry results (Supplementary Materials Table SM4) record paleo-temperatures between 815±18 °C and 1119 ±7 °C although most samples record temperatures between ~850 and 950 °C (Fig. 7A). Two xenoliths contain plagioclase and spinel which coexist over a restrictive range of P–T conditions in most mantle assemblages. Geothermometry on these samples returned relatively low equilibrium temperatures of 850°C (NP-MP05-69) and 874°C (NP-MP05-96). The overall distribution of temperatures suggests that the shallower mantle lithosphere is better represented (i.e. more efficiently sampled) than the deep lithosphere. Conversely, the restricted distribution may simply indicate poor mixing of xenolith populations during dyke transport, in contrast to the efficient mixing processes that attend eruption (Russell and Jones,

2023).

The $\delta^{13}C$ isotopic compositions of xenolith hosted carbonate indicate two groups, relatively enriched ($\delta^{13}C$ ~ -3.4 to -4.4 ‰ (VPDB)) and depleted ($\delta^{13}C$ ~ -5.7 to -6.1 ‰ (VPDB)) (Fig. 6A–B; Table 1), suggesting multiple sources of mantle-equilibrated carbonate within the mantle lithosphere beneath the western margin of the Canadian Cordillera. The two groups have similar oxygen isotopic compositions ($\delta^{18}O$ of 10.3 to 12.5 ‰ (VSMOW)) and record overlapping mantle lithosphere temperatures: 851 to 979 °C (+ one at 1119 °C) *vs*. 849 to 940 °C, respectively.

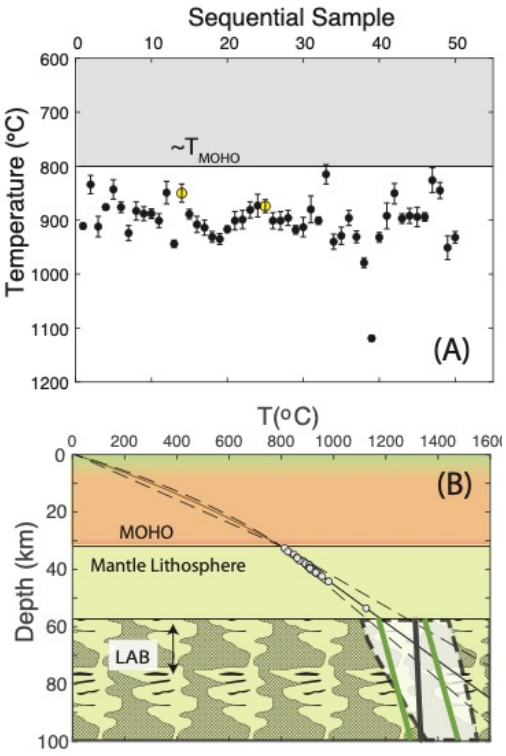

Fig. 7. Geothermometry results and model geotherm for Mt. Preston mantle xenoliths. (A) Mean equilibration BK90 temperatures for peridotite xenoliths (Supplementary Material Table SM4; Brey and Köhler 1990) plotted sequentially in the order they were analyzed with 1σ error based. Yellow symbols denote plagioclase-bearing peridotite samples. (B) Model steady-state geotherm where mantle xenoliths are plotted according to their pressure-dependent equilibration temperatures (see text). Moho depth is fixed by geophysics (34 ± 3 km; Calkins et al., 2010) and the lithosphere/asthenosphere boundary (LAB) is estimated from V_P/V_S data to be at 50–70 km (Calkins et al., 2010). Also shown are: i) the model adiabat (heavy black line) for a potential temperature of 1300 °C after Katsura et al. (2010), ii) reference solidi curves (heavy green lines) for fertile and carbonated peridotite, and iii) a basanite melt field (light shaded field) delimited by liquidus curves for anhydrous and hydrous melts. Model mantle lithosphere geotherms terminate against the adiabat at temperatures of 1313–1320 °C) corresponding to depths of 58–72 km.

7. Discussion

7.1. Geotherm and Carbonated Mantle Lithosphere

Plotting the xenolith equilibration temperatures on a model steady-state geotherm is a means of mapping the distribution of carbonated mantle within the mantle, estimating the minimum thickness of mantle lithosphere, and constraining the depth to the lithosphere-asthenosphere boundary (LAB). Here, we use a one-dimensional model for the lithosphere

494 comprising a crust of known thickness (Z_M) and having constant thermal conductivity (K_1 =
495 2.5 W/m·K), and surface heat flow (qo) and surface temperature (To ~10° C). The crustal
496 layer has an exponential distribution of radiogenic heat producing elements ($A(z) =$
497 $A_O\, e^{-z/Z_M}$; Russell and Kopylova, 1999) and we consider a range of heat production (Ao)
498 values. The underlying mantle lithosphere has constant thermal conductivity (K_2 = 3.2
499 W/m·K) and no radiogenic heat source. The lithospheric crust and mantle are coupled
500 numerically by a common Moho temperature (T_M) and the reduced heat flow (q_M) at the
501 Moho.

502 The temperature distribution as a function of depth (z) in the crust is described by:

503 $$T(z) = T_0 + \frac{q_0\, z}{K_1} + \frac{Ao\, Z_M^2}{K_1}\left(1 - \frac{z}{Z_M} - e^{-z/Z_M}\right) \qquad 0 < z < Z_M \ . \quad (1)$$

504 Values of q_0 are coupled to the form of the heat production equation and dictated by the
505 relationship (Russell and Kopylova, 1999):

506 $$q_0 = 0.3679\, Z_M\, Ao + \frac{(T_M - T_0)\, K_1}{Z_M} \qquad (2)$$

507 and, therefore, also dependent on the depth and temperature of the Moho. The expected
508 steady-state temperature distribution in the mantle lithosphere is described by:

509 $$T(z) = T_M + \frac{[q_0 - 0.6321\, Ao\, Z_M]}{K_2}(z - Z_M) \qquad Z_M < z < Z_a \ . \qquad (3)$$

510 We have assumed a Moho depth (Z_M) of 32 km (Calkins et al., 2010) and an average crustal
511 heat production of 1.6 ±0.8 μW/m^3 (Lewis et al., 2003) which also fixes values of q_0 (Eq. 2).
512 Model values of q_0 for the range of Ao values (0.8 to 2.4 μW/m^3) vary from 63 to 90 mW/m^2
513 which agrees well with average measured values reported for the Canadian Cordillera (76
514 ±21 mW/m^2; e.g., Hyndman, 2017).

515 We assume Moho temperature (T_M) to be equal to or lower than the lowest
516 temperature xenolith (815°C) and have adopted a value of 800°C (Fig. 7). Similarly, the
517 highest temperature xenolith (1119°C) constrains the minimum temperature of the LAB (Fig.
518 7B). A model geotherm is shown in Figure 7B for three separate values of Ao. The model
519 values of q_0 are inversely correlated to values of Ao such that the highest temperature xenolith
520 corresponds to depths of 49 km (low Ao and high q_0) or 58 km (high Ao and low q_0) implying

minimum thicknesses of the mantle lithosphere of 17-26 km. The reduced heat flow at the base of the crust (q_M) would be 61 to 41 mW/m^2 for low to high values of *Ao* (i.e. inverse correlation). These values of q_M correspond to temperature gradients in the mantle of 19 to 13 °C km^{-1}, respectively.

An alternative estimate of lithosphere thickness can be made by extrapolating the model geotherms to intersect the adiabat based on values adopted by Hyndman and Canil, 2021 (after Katsura et al., 2010). The three model geotherms (Fig. 7B) intersect the adiabat at depths of 58 (low *Ao*) to 72 (hi *Ao*) km implying mantle lithosphere thicknesses of between 26 and 40 km and LAB depths between 58-72 km and temperatures of 1310–1320 °C. These results accord well with estimates (65 km and ~1350 ºC) from Hyndman and Canil (2021) and Canil and Hyndman (2023).

The model geotherm shows that carbonate is distributed pervasively throughout the entire mantle lithosphere and that the carbonate is a stable mantle phase over a minimum range of temperatures of 800 to 1120 °C and pressures of 0.9 to 1.7 GPa. The carbonate occurs in several habits, but those habits are insensitive to source temperatures, pressures, and depths. Four samples with granular carbonate have temperatures of 850 to 895 °C, ten xenoliths with carbonate veins have temperatures of 826 to 924 °C, and 37 xenoliths contain both habits and have temperatures of 815 to 1119 °C.

7.2. Significance of mantle carbonate

Primary mantle-derived carbonate is rarely preserved in mantle xenoliths but provides important insights on mantle metasomatism involving carbonatitic melts/fluids. At Mt. Preston, primary carbonate (Mg-calcite) is pervasive and occurs in both lherzolites, websterites, and dunites and the xenoliths preserve strong textural evidence of its mantle equilibration. For example, the intergranular carbonate within the Mt. Preston suite preserves triple-point grain boundaries consistent with textural equilibrium between carbonate and mantle silicates. Other occurrences of carbonate within mantle-derived xenoliths are reported for localities in Argentina (Laurora et al., 2001; Scambelluri et al., 2009), Hungary (Demény et al., 2004; 2010), the Kerguelen Islands (Moine et al., 2004), Spitsbergen (Ionov et al., 1996), the Siberian Craton (Ionov et al., 2018), the East African Rift, Tanzania (Lee et al., 2000), South Africa (Berg, 1986), and the southwest United States (Ducea et al., 2005;

551 Perkins et al., 2006). Most of these occurrences are described as interstitial patches associated
552 with second generation crystallization, or as inclusions within crystals, typically in textural
553 (glass) or isotopic disequilibrium with the host rocks.
554 In addition, mantle carbonate at Mt. Preston is closely associated with sulphides and,
555 together, are found as intergranular patches, in veins, and as inclusion trails within mantle
556 silicates (Fig. 3A–C). Sulphides are a common accessory phase in mantle-derived rocks and
557 are a common component of carbonate melts or carbonate-silicate melts (Ionov et al., 1996).
558 The sulphides found in Mt. Preston mantle xenoliths occur across the full range of
559 equilibration temperatures (i.e. depth) and are found associated with both high and low $\delta^{13}C$
560 groups of carbonate. This occurrence suggests that carbonate and sulphide result from the
561 same enrichment event(s).
562 Chemical compositional features of the Mt. Preston xenoliths are also consistent with
563 a carbonate metasomatic agent. Most of the xenoliths show calcium enrichment relative to
564 aluminum, which has been attributed to cryptic carbonate metasomatism (Peslier et al., 2002).
565 Many REE patterns from the Mt. Preston xenoliths show slight enrichment of the lightest
566 REEs, consistent with the effects of a migrating LREE-rich melt such as carbonatite.
567 Collectively, the petrographic observations and geochemical data strongly support the
568 premise that carbonate and sulphide accessory phases are part of the pre-entrainment mantle
569 paragenesis.
570 Measured $\delta^{18}O$ vs. $\delta^{13}C$ compositions for the Mt. Preston xenolith and dyke
571 carbonates are close to bulk mantle compositions and distinct from the wall rock carbonates
572 (Fig. 6B). In fact, the $\delta^{13}C$ and $\delta^{18}O$ isotopic compositions of Mt. Preston carbonate are closer
573 to primary mantle compositions than many other occurrences of mantle-hosted carbonates
574 (Fig. 6B; Lee et al., 2000; van Achterbergh et al., 2002; Demény et al., 2004; Ducea et al.,
575 2005; Perkins et al., 2006). Oxygen isotopic compositions can be more easily re-equilibrated,
576 yet the measured $\delta^{18}O$ values show no indication of chemical mixing between sources (i.e.
577 xenolith, dyke, wall rock) and no signs of meteoric alteration.
578 $\delta^{13}C$ values for the Mt. Preston peridotite xenoliths are similar to carbonate-bearing
579 mantle xenoliths from New Mexico (Lee et al., 2000), however, their more mantle-like $\delta^{18}O$
580 values suggest better preservation of primary carbonate. Carbon isotopes are less susceptible

581 to re-equilibration and the Mt. Preston mantle-carbonate samples define two distinct groups
582 suggesting at least two carbonate-sulphide melt enrichment events. The concept of multiple
583 enrichment events is further supported by the $^{87}Sr/^{86}Sr$ isotopic data which shows the two
584 $\delta^{13}C$-defined populations to have distinct $^{87}Sr/^{86}Sr$ compositions and to be different from the
585 dyke. The $^{87}Sr/^{86}Sr$ data for the dyke carbonate could be a mix of $^{87}Sr/^{86}Sr$ compositions
586 derived from the dyke silicates and the xenolith carbonate thereby preserving evidence for a
587 magma charged with CO_2 derived from mantle-derived (i.e. xenolith) carbonate (see below).

588 7.3. Source of Carbonatite Metasomatism

589 Studies of the mantle lithosphere underlying the Canadian Cordillera have shown it
590 to be relatively uniform in composition, thermal regime, and age (e.g., Francis et al., 2010
591 and references therein). Rhenium-osmium dating of lithospheric mantle-derived xenoliths
592 (Peslier et al., 2000) has recovered Proterozoic model ages across the Canadian Cordillera,
593 consistent with melt depletion events occurring within a short timeframe for the Cordilleran
594 lithospheric mantle. Whether autochthonous or allochthonous this indicates a common
595 melting history for, at least, the lithospheric mantle underlying the southeast Canadian
596 Cordillera. This result precludes the suggestion of a simple extension of cratonic crust
597 coupled to its own lithospheric mantle residing beneath the eastern Cordillera, as the mantle
598 lithosphere in that region appears to be much younger than the wedge of cratonic crustal
599 basement that overlies it (Peslier et al., 2000).

600 The Mt. Preston xenolith suite is in a unique geographic location compared to other
601 BC cordilleran xenolith localities which are predominantly within the Intermontane belt.
602 They are also the only mantle peridotite xenoliths in the BC cordillera that preserve
603 metasomatic carbonates (and associated sulphides). Furthermore, these carbonated mantle
604 xenoliths are the only ones reported from the Pacific Coast Ranges of the western margin of
605 North America. The carbonates and sulphides are texturally undisturbed suggesting that the
606 metasomatic event was the last event to occur prior to entrainment by the 19 Ma basanite
607 magma. This suggests a different history and processes involving a geographically restricted
608 enrichment process that probably involved metasomatic agents related to subduction of
609 oceanic crust along the central western margin of BC.

610 One possible contribution for carbonatitic metasomatism into the mantle lithosphere

611 is the subduction of carbonate in sediments from the down going slab. Subducting slab-
612 related enrichment agents have been interpreted for other carbonate bearing xenolith suites
613 (e.g. Laurora et al., 2001; Demény et al., 2004; Ducea et al., 2005; Perkins et al., 2006).
614 Decarbonation reactions in subducting plates can occur at higher temperatures than
615 dehydration reactions, based on experimental and thermodynamic data (Yaxley and Green,
616 1994; Ducea et al., 2005 and references therein), or the silicate and carbonate melts may be
617 immiscible resulting in separation. Subduction-related metasomatism has been considered
618 for xenolith suites from northwest BC and southwest Yukon based on incompatible trace
619 element enrichments, although no metasomatic phases were observed in those rocks (Shi et
620 al., 1998; Peslier et al., 2000). If subduction-related enrichment during Coast Plutonic
621 Complex magmatism is postulated as the source for the carbonates and sulphides in the Mt.
622 Preston suite, the sites in northwest BC and southwest Yukon could be expected to show this
623 as well. However, several of these sites are interpreted to overlie anomalously hot
624 asthenosphere interpreted as a Tertiary to recent thermal event (Frederiksen et al., 1998; Shi
625 et al., 1998); at the interpreted P–T range for these rocks little isobaric heating (≤50 °C) is
626 required to make crystalline calcite unstable.
627 Mt. Preston occupied an arc to back-arc location during the duration of Coast Plutonic
628 Complex magmatism history. Based on tectonic models (van der Heyden, 1992; Monger et
629 al., 1994; Gehrels et al., 2009), this would restrict the timing of the enrichment event(s) from
630 at earliest, Jurassic time to ~50 Ma when Coast Belt magmatism waned; subduction ended
631 ~40 Ma, although the margin of the subducted slab persisted to ~35 Ma beneath the area
632 (Madsen et al., 2006). However, for metasomatic enrichment to have occurred before 90–85
633 Ma the mantle lithosphere under Mt. Preston would have had to be thermally and texturally
634 unaffected by the accretion of terranes of the Insular Belt into Stikinia–Yukon Tanana (e.g.,
635 Monger et al., 1982; Gehrels et al., 2009).
636 The $^{87}Sr/^{86}Sr$ values for Mt. Preston samples are slightly more radiogenic than
637 expressed by the eastern BC xenolith suites. The more radiogenic $^{87}Sr/^{86}Sr$ ratios might be
638 indicative of carbonatite metasomatism or the lower $^{87}Sr/^{86}Sr$ ratios for the eastern BC
639 xenoliths could reflect the region's proximity to the North American Craton margin. Isotopic
640 evidence suggests that the Cordilleran lithosphere may not be as uniform as previously shown

(Peslier et al., 2000; Francis et al., 2010). In particular, the carbonated peridotite samples from Mt. Preston imply important compositional variations within the Canadian Cordilleran mantle lithosphere that inform on the mantle's volatile budget (carbon), the fate of subducted carbon, and its release during volcanism (discussed in section 7.4). The stability of carbonate, in the mantle, for example, has been shown to be redox controlled (e.g., Frost & McCammon, 2008), suggesting variations in the oxidation state of mantle material beneath the Intermontane–Coast Belt margin in the western Cordillera.

7.4. Carbonate Preservation and Ascent

Carbonated peridotitic mantle is the common source for a wide variety of mantle-derived magmas including carbonatites, nephelinites, basanites, melilitites, and kimberlites (e.g., Dasgupta et al. 2013). Given Earth's abundance of these Si-undersaturated, CO_2-rich magmas it is surprising that carbonate-bearing samples of mantle lithosphere are relatively rare. This discrepancy led Canil (1990) to perform a series of decompression experiments designed to explore the carbonate stability during ascent and to assert that carbonate decomposes during decompression at rates (1.5–3 GPa h^{-1}) exceeding feasible magma ascent velocities (12–25 m s^{-1}).

This raises the question of how the carbonate in these xenoliths was preserved during ascent of the Mt. Preston basanite magma. All samples of the mantle beneath Mt. Preston were carbonated and equilibrated at pressures less than 2 GPa and at temperatures lower than the basanite magma (<1250°C). In this environment, carbonate can be destroyed in at least three ways: i) by solid state reaction to produce a non-carbonate assemblage, ii) by decomposition to a fluid or gas driven by changes in pressure, temperature, or P_{CO2} (Canil 1990; Escardino et al., 2013; Frost & McCammon, 2008), or iii) by dissolution or assimilation in a silicate melt (Edwards and Russell, 1998). To preserve the carbonate and sulphides in the xenoliths, transport rates of the xenoliths must have exceeded rates of thermal-chemical processes promoting carbonate destruction (i.e. decomposition, melt infiltration, etc.).

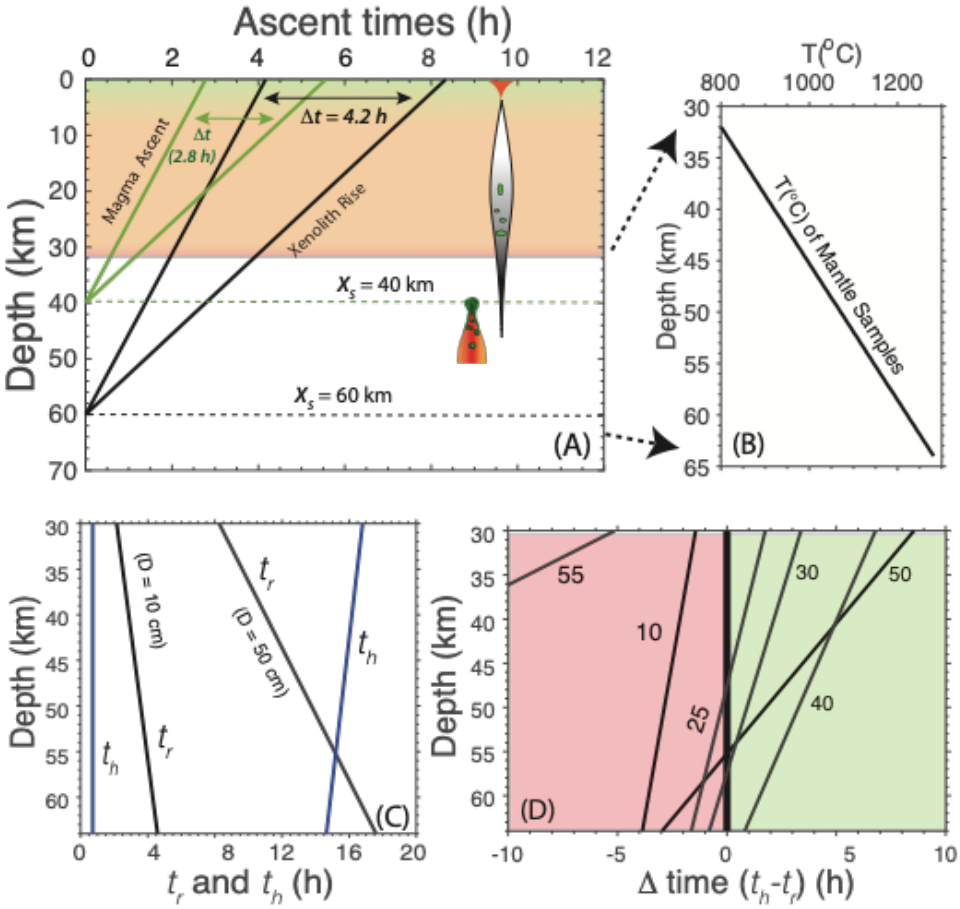

Fig. 8. Residence (t_r) and heating (t_h) times for mantle xenoliths within basanite magma. (A) Times for ascent of magma rising from 40 (2.7 h) and 60 (4.1 h) km depth at velocities of 4 m s^{-1} and the implied residence times (5.5 h and 8.4h) for a 25 cm diameter xenolith due to lagging (Russell and Jones, 2023). (B) Mantle temperature array with depth based on model geotherm (Fig. 7B). (C) Comparison of xenolith residence times (t_r) to times to heat (t_h) the core of two xenoliths (D=10 and 50 cm) to 1300°C as a function of sample depth. Smaller xenoliths (D=10 cm) are heated to their core regardless of source depth; larger xenoliths (D=50 cm) rise faster than they are heated except when sourced from the base of the mantle lithosphere. (D) Values of $(t_h - t_r)$ as a function of source depth and xenolith size (see labels). Positive values of $(t_h - t_r)$ are consistent with carbonate survival (green shading) whilst negative values indicate full heating of xenoliths and possible decomposition of xenolith-hosted carbonate (red shading).

There is every evidence that the basanite magma transited the mantle lithosphere rapidly. The basanite is essentially aphyric (i.e. no phenocrysts) indicating that near liquidus temperatures (~1250°C) were maintained throughout transport, implying little loss of enthalpy; ascent rates exceeded rates of conductive cooling to the wall rocks. The basanite dyke also transported dense mantle xenoliths (Fig. 2) sourced from depths of 70–30 km to within several kilometers of the Earth's surface. Several of the largest xenoliths are ~50 cm

687 in diameter. The abundance and size range of xenoliths carried by a low viscosity melt within
688 a relatively narrow dyke (1–3 m) also support a relatively high ascent rate (e.g., Sparks et al.,
689 2004). For our example calculations below we adopt a physically reasonable value ~4 m s^{-1}
690 (see Sparks et al., 2004; Russell and Jones, 2023).
691 There are two main arguments for the preservation of the carbonate in this suite of
692 mantle xenoliths. The first concerns the thermal history of the xenoliths from the depth of
693 sampling to the shallow crust. Decomposition of carbonate is strongly dependent on
694 temperature; as xenoliths are heated above their ambient mantle temperatures by the host
695 basanite, rates of carbonate decomposition will increase (L'vov, 2007; Escardino et al., 2013).
696 We have modelled the heating times (t_h) of the mantle xenoliths and compared those times
697 to their residence times (t_r) at a prescribed ascent rate (V_m ~4 m s^{-1}; Fig. 8A). Xenolith
698 residence times are dictated by magma rise rate, their settling rates (i.e. size of xenolith), and
699 their source depth (Fig. 8B; Russell and Jones, 2023). Values of t_r are greatest for large
700 xenoliths sourced from greatest depths (Fig. 8A) whilst V_m sets limits on the maximum size
701 of xenolith that can be carried. Heating times are the times required to heat spherical xenoliths
702 of different sizes to a core temperature > 1250°C assuming conductive heating (e.g., Crank,
703 1975, Eq. 6.19) and an initial temperature based on their position along the geotherm (i.e.
704 depth-temperature; Fig. 8B).
705 There is a window in terms of xenolith size and source depth where carbonate is
706 preserved (Fig. 8D). Carbonate preservation is favoured when $t_h > t_r$. Small xenoliths (i.e. D
707 < 10 cm) typically have $t_h < t_r$ regardless of sample depth because heating times are short
708 (Fig. 8C). In contrast, 50 cm diameter xenoliths have substantial heating times relative to
709 their rise rates ($t_r < t_h$) except when sourced near the LAB; there transit times are greatest,
710 and the ambient temperature is highest thereby reducing t_h values. However, slightly larger
711 xenoliths (D ~ 55 cm) are settling more rapidly and have high values of t_r, such that $t_r >> t_h$
712 regardless of sample depth (Fig. 8D). For minimum magma ascent rates of 4 m s^{-1}, xenoliths
713 that are between 30 and 40 cm in size are optimal for preserving carbonate (Fig. 8D).
714 The second way in which carbonate decomposition is mitigated relates to the intrinsic
715 volatile content of the host magma. Carbonate decomposition rates are strongly dependent
716 on the composition of ambient atmosphere; high values of P_{CO2} cause a hyperbolic decrease

717 in carbonate decomposition rate (L'vov, 2007). Experimental data of Escardino et al. (2013)
718 showed calcite decomposition in a CO_2 atmosphere to practically stop at temperatures < 875
719 °C; at higher temperatures decomposition rates dropped by > 80%. The basanite dyke
720 contains magmatic groundmass carbonate and is vesicular indicating it was CO_2-volatile rich.
721 Despite the low solubility of CO_2 at crustal pressures, the magma trapped in the dyke was
722 not fully degassed but, rather, remained enriched in CO_2. The ascent rates were sufficiently
723 high to effectively suppress efficient degassing of CO_2 implying a high partial pressure of
724 CO_2 throughout transport that would inhibit carbonate decomposition.

725 Lastly, all samples of mantle lithosphere from beneath Mt. Preston are carbonated
726 regardless of depth. It is, therefore, likely that the magma was able to mechanically scavenge
727 and chemically assimilate mantle-derived carbonate. In several studies of xenoliths
728 containing carbonate, authors noted that the host lavas also contained carbonate and
729 suggested that the magmas preferentially assimilated carbonate from mantle material to
730 become significantly CO_2 enriched (e.g., Ionov et al., 1996; Lee et al., 2000; Laurora et al.,
731 2001). Disaggregation of carbonated peridotite xenoliths during transport represents an
732 efficient mechanism for liberation of accessory carbonate leading to increased CO_2 solubility
733 or suppression of degassing of the rising magma. The additional dissolved or exsolved CO_2
734 content would increase magma buoyancy, support higher ascent rates for, both, the magma
735 and its entrained xenoliths, thereby, enhancing carbonate preservation. The carbon, oxygen,
736 and strontium isotopic compositions of the dyke and xenolith carbonate are consistent with
737 this process. For example, the carbonate sampled from the basanite dyke has a $\delta^{13}C$
738 composition within the range of the sampled mantle xenoliths, and has a $^{87}Sr/^{86}Sr$
739 composition between the dyke silicate minerals and the xenolith carbonate.

740 **8. Conclusions**

741 The 19 My basanite dyke exposed near Mt. Preston, British Columbia intrudes
742 metavolcanic rocks (Hazelton Group) of the western Intermontane Belt and is situated
743 within 40 km of Coast Belt. The dyke contains abundant spinel-bearing peridotite (mainly
744 lherzolite) xenoliths from the underlying Cordilleran mantle. The xenolith suite is unique
745 for preserving primary, mantle-equilibrated magnesian calcite as an accessory phase
746 commonly in association with sulphides (pentlandite and chalcopyrite). Two-pyroxene

thermometry (N=51) returned a range of paleo-temperature estimates limiting the Moho temperature to ≤ 815 ºC and the LAB temperature to ≥ 1120 ºC. A model geotherm, coupled with the geothermometry and projected to the mantle adiabat, constrains the mantle lithosphere to a thickness of 26 to 40 km, and the LAB to a depth of 58 to 72 km and temperature of 1310–1320 ºC (see also Hyndman and Canil, 2021). The thermometry also shows that accessory carbonate and sulphide phases are stable throughout mantle lithosphere at temperatures of ~800 –1120ºC corresponding to pressures (i.e. depths) of ~1–1.7 GPa. The carbonate-sulphide assemblage provides strong evidence for pervasive metasomatism of an earlier melt-depleted mantle lithosphere involving at least two isotopically distinct carbonatitic fluids with associated monosulphides (rather than hydrous silicate fluids). The metasomatic event derived from subduction of oceanic crust beneath the western margin of the Canadian Cordillera during Coast Plutonic Belt magmatism, when Mt. Preston was in an arc to back arc position (between ~90 and 35 Ma). Rapid magma transport rates combined with a high intrinsic P_{CO2}, sustained by scavenging of carbonated mantle lithosphere, provided the means to preserve the accessory carbonate within these entrained fragments of mantle lithosphere.

Acknowledgements

This research was funded by the Natural Sciences and Engineering Research Council (NSERC) Discovery Grant held by JKR and the NSERC Collaborative Research Opportunities (CRO) grant (BATHOLITHS). NP acknowledges research grants awarded by the Geological Society of America and the Mineralogical Association of Canada.

References

Asimow, P.D., Ghiorso, M.S., 1998. Algorithmic modifications extending MELTS to calculate subsolidus phase relations. Am. Min. 83, 1127-1131.

Barker, D.S., 1996. Consequences of recycled carbon in carbonatites. Can. Min. 34, 373-387.

Berg, G.W., 1986. Evidence for carbonate in the mantle. Nature 324, 50-51.

Bodinier, J.L., Dupuy, C., Dostal, J., 1988. Geochemistry and petrogenesis of Eastern Pyrenean peridotites. Geochim. Cosmochim. Acta. 52, 2893-29.

Boyd, F. R., 1989. Compositional distinction between oceanic and cratonic lithosphere.

779 Earth Planet. Sci. Lett. 96, 15-26.
780 Brey, G. P., Köhler, T., 1990. Geothermobarometry in Four-phase Lherzolites II. New
781 Thermobarometers, and Practical Assessment of Existing Thermobarometers. J.
782 Petrol. 31, 6, 1353-1378.
783 Calkins, J. A., Zandt, G., Girardi, J., Dueker, K., Gehrels, G. E., Ducea, M. N., 2010.
784 Characterization of the crust of the Coast Mountains Batholith, British Columbia,
785 from P to S converted seismic waves and petrologic modeling. Earth Planet. Sci.
786 Lett. 289, 145-155.
787 Canil, D., 1990. Experimental study bearing on the absence of carbonate in mantle-derived
788 xenoliths. Geology 18, 1011-1013.
789 Canil, D., Scarfe, C.M., 1989. Origin of phlogopite in mantle xenoliths from Kostal Lake,
790 Wells Gray Park, British Columbia. J. Petrol. 30, 1159-1179.
791 Canil, D., Hyndman, R.D., 2023. Equilibration depth and temperature of Neogene alkaline
792 lavas in the Cordillera of Alaska and Canada as a constraint on the lithosphere–
793 asthenosphere boundary. Can. J. Earth Sci. 60, 1206-1222.
794 Clinton R. N., Mayeda T. K., 1963. The use of bromine pentafluoride in the extraction of
795 oxygen from oxides and silicates for isotopic analysis. Geochimica et
796 Cosmochimica Acta 27, 43-52.
797 Crank, J., 1975. The Mathematics of Diffusion. 2nd Edition, Oxford University Press,
798 London
799 Dasgupta, R., Mallik, A., Tsuno, K., et al. 2013. Carbon-dioxide-rich silicate melt in the
800 Earth's upper mantle. Nature 493, 211–215.
801 Deines, P., 2002. The carbon isotope geochemistry of mantle xenoliths. Earth-Science
802 Reviews 58, 247-278.
803 Delpech, G., Lorand, J. P., Grégoire, M., Cottin, J. Y., O'Reilly, S. Y., 2012. In-situ
804 geochemistry of sulfides in highly metasomatized mantle xenoliths from Kerguelen,
805 southern Indian Ocean. Lithos 154, 296-314.
806 Demény, A., Vennemann, T. W., Hegner, E., Nagy, G., Milton, J. A., Embey-Isztin, A.,
807 Homonnay, Z., Dobosi, G., 2004. Trace element and C–O–Sr–Nd isotope evidence
808 for subduction-related carbonate–silicate melts in mantle xenoliths (Pannonian
809 Basin, Hungary). Lithos 75, 89-113.
810 Demény, A., Dallai, L., Frezzotti, M.-L., Vennemann, T.W., Embey-Isztin, A., Dobosi, G.,
811 Nagy, G., 2010. Origin of CO_2 and carbonate veins in mantle-derived xenoliths in
812 the Pannonian Basin. Lithos 117, 172-182.
813 Ducea, M. N., Saleeby, J., Morrison, J., Valencia, V. A., 2005. Subducted carbonates,
814 metasomatism of mantle wedges, and possible connections to diamond formation:
815 An example from California. Am. Mineral. 90, 864-870.
816 Edwards, B., Russell, J. K., 1998. Time scales of magmatic processes: new insights from
817 dynamic models for magmatic assimilation. Geology 26, 1103–1106.
818 Edwards, B., Russell, J. K., 2000. Distribution, nature, and origin of Neogene-Quaternary
819 magmatism in the northern Cordilleran volcanic province, Canada. Geol. Soc. Am.
820 Bull. 112, 1280–1295.
821 Escardino, A., García-Ten, J., Feliu, C., Saburit, A., Cantavella, V., 2013. Kinetic study of
822 the thermal decomposition process of calcite particles in air and CO_2 atmosphere. J.
823 Ind. Eng. Chem. 19, 886-897.

824 Francis, D., Minarik W., Proenza Y., Shi, L., 2010. An overview of the Canadian
825 Cordilleran lithospheric mantle. Can. J. Earth Sci. 47, 353-368.
826 Francis, D., Ludden, J., 1995. The signature of amphibole in mafic alkaline lavas, a study in
827 the Northern Canadian Cordillera. J. Petrol. 36, 1171-1191.
828 Frederiksen, A. W., Bostock, M. G., VanDecar, J. C., Cassidy, J. F., 1998. Seismic
829 structure of the upper mantle beneath the northern Canadian Cordillera from
830 teleseismic travel-time inversion. Tectonophys. 294, 43-55.
831 Frost, D. J., McCammon, C. A., 2008. The redox state of Earth's mantle. Annu. Rev. Earth
832 Planet. Sci., 36, 389-420.
833 Gehrels, G., Rusmore, M., Woodsworth, G., Crawford, M., Andronicos, C., Hollister, L.,
834 Patchett, J., Ducea, M., Butler, R., Klepeis, K., Davidson, C., Friedman, R.,
835 Haggart, J., Mahoney, B., Crawford, W., Pearson, D., Girardi, J., 2009. U-Th-Pb
836 geochronology of the Coast Mountains batholith in north-coastal British Columbia:
837 constraints on age and tectonic evolution. Geol. Soc. Am. Bull. 121, 1341-1361.
838 Ghent, E.D., Edwards, B.R., Russell, J.K., 2019. Pargasite-bearing vein in spinel lherzolite
839 from the mantle lithosphere of the North America Cordillera. Can. J. Earth Sci. 56,
840 870-885.
841 Gordee S. M., Mortensen J. K., Mahoney J. B., Hooper R. L. 2005. Volcanostratigraphy,
842 lithogeochemistry and U-Pb geochronology of the upper Hazelton Group, west-
843 central British Columbia: implications for Eskay Creek – type VMS mineralization
844 in southwest Stikinia. In Geological Fieldwork, 2004, British Columbia Ministry of
845 Energy, Mines and Petroleum Resources, Paper 2005-1, pp. 311–322.
846 Harder, M., Russell, J. K., 2006. Thermal state of the upper mantle beneath the Northern
847 Cordilleran Volcanic Province (NCVP), British Columbia, Canada. Lithos 87, 1-
848 22.
849 Harmon, R. S., Hoefs, J., 1995. Oxygen isotope heterogeneity of the mantle deduced from
850 global ^{18}O systematics of basalts from different geotectonic settings. Contrib.
851 Mineral. Petrol. 120, 95-114. 126
852 Hyndman, R.D., 2017. Lower-crustal flow and detachment in the North American
853 Cordillera: a consequence of Cordillera-wide high temperatures. Geophys. J. Int.
854 209, 1779–1799, https://doi.org/10.1093/gji/ggx138
855 Hyndman, R.D., Canil, D., 2021. Geophysical and geochemical constraints on Neogene-
856 Recent volcanism in the North American Cordillera Geochem. Geophys. Geosys.
857 22, e2021GC009637. https://doi.org/10.1029/2021GC009637
858 Ionov, D. A., O'Reilly, S. Y., Genshaft, Y. S., Kopylova, M. G., 1996. Carbonate-bearing
859 mantle peridotite xenoliths from Spitsbergen: phase relationships, mineral
860 compositions and trace-element residence. Contrib. Mineral. Petrol. 125, 375-392.
861 Ionov, D.A., Shirey, S.B., Weis, D., Brugmann, G., 2006. Os–Hf–Sr–Nd isotope and PGE
862 systematics of spinel peridotite xenoliths from Tok, SE Siberian craton: Effects of
863 pervasive metasomatism in shallow refractory mantle. Earth Planet. Sci. Lett. 241,
864 47-64.
865 Ionov, D.A., Doucet, L.S., Xu, Y., Golovin, A.V., Oleinikov, O.B., 2018. Reworking of
866 Archean mantle in the NE Siberian craton by carbonatite and silicate melt
867 metasomatism: Evidence from a carbonate-bearing, dunite-to-websterite xenolith
868 suite from the Obnazhennaya kimberlite. Geochim. Cosmochim. 224, 132-153.

869 Katsura, T., Yoneda, A., Yamazaki, D., Yoshino, T., Ito, E., 2010. Adiabatic temperature
870 profile in the mantle: Phys. Earth Planet. Inter. 183, 212–218.
871 Keller, J., Hoefs, J., 1995. Stable isotope characteristics of recent natrocarbonatites from
872 Oldoinyo Lengai. In: Carbonatite volcanism: Oldoinyo Lengai and the petrogenesis
873 of natrocarbonatites. (eds. K. Bell and J. Keller). Springer, Berlin. pp. 113-123.
874 Laurora, A., Mazzucchelli, M., Rivalenti, G., Vannucci, R., Zanetti, A., Barbieri, M. A.,
875 Cingolani, C. A., 2001. Metasomatism and melting in carbonated peridotite
876 xenoliths from the mantle wedge: The Gobernador Gregores Case (Sothern
877 Patagonia). J. Petrol. 42, 1, 69-87.
878 Lee, C., Rudnick, R. L., McDonough, W. F., Horn I., 2000. Petrologic and geochemical
879 investigation of carbonates in peridotite xenoliths from northeastern Tanzania.
880 Contrib. Mineral. Petrol. 139, 470-484.
881 Lewis, T. J., Hyndman, R. D., Fluck, P., 2003. Heat flow, heat generation, and crustal
882 temperatures in the northern Canadian Cordillera: Thermal control of tectonics. J.
883 Geophys. Res. 108, B6, 16-1 – 16-18.
884 L'vov, B.V., 2007. Thermal Decomposition of Solids and Melts: New Thermochemical
885 Approach to the Mechanism, Kinetics and Methodology. Dordrecht: Springer
886 Netherlands, http://dx.doi.org/10.1007/978-1-4020-5672-7.
887 Madsen, J. K., Thorkelson, D. J., Friedman, R. M., Marshall, D. D., 2006. Cenozoic to
888 Recent plate configurations in the Pacific Basin: Ridge subduction and slab window
889 magmatism in western North America. Geosphere 2, 1, 11-34.
890 Mahoney J. B., Hooper R. L., Gordee S. M., Haggart J. W., Mortensen J. K. 2005. Initial
891 evaluation of bedrock geology and economic mineralization potential of southern
892 Whitesail Lake map area (NTS 093E/02, 03), west-central British Columbia. In
893 Geological Fieldwork, 2004, British Columbia Ministry of Energy, Mines and
894 Petroleum Resources, Paper 2005-1, pp. 291–299.
895 McDonough, W. F., Sun, S., 1995. The composition of the Earth. Chem. Geol. 120, 223-
896 253.
897 Moine, B. N., Gregoire, M., O'Reilly, S. Y., Delpech, G., Sheppard, S. M. F., Lorand, J. P.,
898 Renac, C., Giret, A., Cottin, J. Y., 2004. Carbonatite melt in oceanic upper mantle
899 beneath the Kerguelen Archipelago. Lithos 75, 239-252.
900 Monger, J., Price, R. A., Tempelman-Kluit, D. J., 1982. Tectonic accretion and the origin of
901 the two major metamorphic and plutonic welts in the Canadian Cordillera. Geology
902 10, 70–75.
903 Monger, J., van der Heyden, P., Journeay, J. M., Evenchick, C. A., Mahoney, J. B., 1994.
904 Jurassic-Cretaceous basins along the Canadian Coast Belt: Their bearing on pre-
905 mid- Cretaceous sinistral displacements. Geology 22, 175-178.
906 Pearson, D. G., Canil, D., Shirey, S.B. and Carlson. R. W. 2003. Mantle samples included
907 in volcanic rocks: Xenoliths and diamonds, in (Eds. H. D. Holland, K. K. Turekian)
908 Treatise on Geochemistry. Pergammon, 171-275. doi.org/10.1016/B0-08-043751-
909 6/02005-3.
910 Perkins, G. B., Sharp, Z. D., Selverstone, J., 2006. Oxygen isotope evidence for subduction
911 and rift-related mantle metasomatism beneath the Colorado Plateau-Rio Grande rift
912 transition. Contrib. Mineral. Petrol. 151, 633-650.
913 Peslier, A. H., Reisberg, L., Ludden, J., Francis, D., 2000. Os isotopic systematics in

914 mantle xenoliths; age constraints on the Canadian Cordillera lithosphere. Chem.
915 Geol. 166, 85-101.
916 Peslier, A. H., Francis, D., Ludden, J., 2002. The lithospheric mantle beneath continental
917 margins: Melting and melt-rock reaction in Canadian Cordillera xenoliths. J. Petrol.
918 43, 11, 2013-2047.
919 Peterson, N.D., Russell, J.K., Mahoney, J.B. 2006. Mantle-Derived Peridotite Xenoliths
920 from the Western Intermontane Belt, Whitesail Lake map area (NTS 093E),
921 Western BC. Geological Fieldwork, Ministry of Energy, Mines and Petroleum
922 Resources Paper 2006-1, 153-161.
923 Peterson, N.D., 2010. Carbonated mantle lithosphere in the western Canadian Cordillera.
924 University of British Columbia. doi.org/10.14288/1.0052818
925 Polat, A., Frei, R., Longstaffe, F.J., Thorkelson, D.J., Friedman, E., 2018. Petrology and
926 geochemistry of the Tasse mantle xenoliths of the Canadian Cordillera: A record of
927 Archean to Quaternary mantle growth, metasomatism, removal, and melting,
928 Tectonophys. 737, 1-26.
929 Pouchou J. L., Pichoir F., 1985. PAP $\phi(\rho Z)$ procedure for improved quantitative
930 microanalysis. Microbeam Analysis 1985, 104-106.
931 Rielli, A., Tomkins, A.G., Nebel, O., Brugger, J., Etschmann, B., Evans, K.A., et al., 2022.
932 Incipient metal and sulfur extraction during melting of metasomatised mantle. Earth
933 Planet. Sci. Lett. 599, 117850, https://doi.org/10.1016/j.epsl.2022.117850.
934 Rudnick, R. L., McDonough, W. F., Chappell B. W., 1993. Carbonatite metasomatism in
935 the northern Tanzanian mantle: petrographic and geochemical characteristics. Earth
936 Planet. Sci. Lett. 114, 463-475.
937 Russell, J. K., Kopylova, M. K., 1999. A steady-state conductive geotherm for the north
938 central Slave, Canada: inversion of petrological data from the Jericho kimberlite
939 pipe. J. Geophys. Res. 104, 7089–7101.
940 Russell, J.K., Jones, T.J., 2023. Transport and eruption of mantle xenoliths creates a
941 lagging problem. Comm. Earth Environ. 4, 177. doi.org/10.1038/s43247-023-
942 00843-0
943 Scambelluri, M., Vannucci, R., De Stefano, A., Preite-Martinez, M., Rivalenti, G., 2009.
944 CO_2 fluid and silicate glass as monitors of alkali basalt/peridotite interaction in the
945 mantle wedge beneath Gobernador Gregores, Southern Patagonia. Lithos 107, 121-
946 133.
947 Shi, L., Francis, D., Ludden, J., Frederiksen, A., Bostock, M., 1998. Xenolith evidence for
948 lithospheric melting above anomalously hot mantle under the northern Canadian
949 Cordillera. Contrib. Mineral. Petrol. 131, 39-53.
950 Sparks, R. S. J., Baker, L., Brown, R.J., Field, M., Schumacher, J., Stripp, G., Walters, A.,
951 2006. Dynamical constraints on kimberlite volcanism. J. Volc. Geotherm. Res., 155,
952 18-48, doi.org/10.1016/j.jvolgeores.2006.02.010.
953 Sun, C., Liang, Y., 2013. The importance of crystal chemistry on REE partitioning between
954 mantle minerals (garnet, clinopyroxene, orthopyroxene, and olivine) and basaltic
955 melts. Chem. Geol. 358, 23-36.
956 Sun, M., Armstrong, R.L., Maxwell, R.J., 1991. Proterozoic mantle under Quesnellia:
957 variably reset Rb–Sr mineral isochrons in ultramafic nodules carried up in Cenozoic
958 volcanic vents of the southern Omineca Belt. Can. J. Earth Sci. 28, 1239-1253.

959 Taylor Jr., H. P., Frechen, J., Degens, E. T. 1967. Oxygen and carbon isotope studies of
960 carbonatites from the Laacher See district, West Germany, and the Alnö district,
961 Sweden. Geochim. Cosmochim. Acta 31, 407-430.
962 Van Achterbergh, E., Griffin, W. L., Ryan, C. G., O'Reilly, S. Y., Pearson, N. J., Kivi, K.,
963 Doyle B. J., 2002. Subduction signature for quenched carbonatites from the deep
964 lithosphere. Geology 30, 8, 743-746.
965 Van der Heyden, P., 1992. A middle Jurassic to early Tertiary Andean-Sierran arc model
966 for the Coast Belt of British Columbia. Tectonics 11, 1, 82-97.
967 Warren, J.M., 2016. Global variations in abyssal peridotite compositions. Lithos 248–251,
968 193-219.
969 Wasylenki, L.E., Baker, M.B., Kent, A.J., Stolper, E.M., 2003. Near-solidus melting of the
970 shallow upper mantle: Partial melting experiments on depleted peridotite. J. Petrol.
971 44 1163–1191.
972 Wheeler, J. O., Brookfield, A. J., Gabrielse, H., Monger, J. W. H., Tipper, H. W.,
973 Woodsworth, G. J., 1991. Terrane Map of the Canadian Cordillera: Geological
974 Survey of Canada Map 1713A, scale 1:2,000,000.
975 Workman, R.K., Hart, S.R., 2005. Major and trace element composition of the depleted
976 MORB mantle (DMM). Earth Planet. Sci. Lett. 231, 53-72.
977 Yaxley, G. M., Green, D. H., 1994. Experimental demonstration of refractory carbonate
978 bearing eclogite and siliceous melt in the subduction regime. Earth Planet. Sci. Lett.
979 128, 313-325.
980 Yaxley, G. M., Crawford, A. J., Green D. H., 1991. Evidence for carbonatite metasomatism
981 in spinel peridotite xenoliths from western Victoria, Australia. Earth Planet. Sci.
982 Lett. 107, 305-317.
983 Yaxley, G. M., Green D. H., Kamenetsky, V. 1998. Carbonatite Metasomatism in the
984 Southeastern Australian Lithosphere, J. Petrol. 39, 1917–1930.

Table SM1. Whole rock geochemical compositions of Mt. Preston basanite dike including major, trace and rare-earth element contents and radiogenic and stable isotopic data. Dataset also includes isotopic data for carbonate fractions (CF) in whole rock (WR) powders. Values also reported for standards (e.g., SRM987) and for duplicates and replicates[1]

Major Elements (wt.%)

Sample	MP05-1	MP05-3	MP05-3[2]
Rock Type[1]	BAS	BAS	BAS
SiO_2	43.11	45.47	45.46
TiO_2	2.70	2.27	2.27
Al_2O_3	12.99	13.55	13.61
FeO_{Total}	12.09	12.04	12.07
MnO	0.182	0.177	0.179
MgO	10.91	10.13	10.25
CaO	10.59	9.82	9.75
Na_2O	2.33	2.85	2.88
K_2O	1.40	1.02	1.03
P_2O_5	0.48	0.35	0.35
H_2O^+	0.74	0.41	0.40
H_2O^-	0.67	0.32	0.24
CO_2	0.70	0.14	0.10
Total	98.89	98.54	98.60
LOI	1.98	1.19	0.93

Trace and Rare Earth Elements (ppm)

Rb	28.3	16.6	16.8
Sr	691.0	520.0	514.0
Ba	521	332	342
V	256	235	241
Cr	281	335	348
Co	64	56	62
Ni	256	214	218
Zn	83	78	80
Cu	93	84	83
Ga	18.7	18.2	17.1
Y	21.7	21.6	21.2
Zr	173.5	118.3	116.7
Nb	32.2	18.7	18.2
Th	3.7	2.5	1.9
U	3.9	2.5	2.7
La	24.94	16.96	19.04
Ce	49.60	35.61	39.88
Pr	6.37	4.94	5.46
Nd	26.91	21.68	24.37
Sm	5.77	5.16	5.67
Eu	2.034	1.756	1.993
Gd	4.38	3.97	4.47
Tb	0.813	0.764	0.861
Dy	4.38	4.38	4.97
Ho	0.741	0.823	0.924
Er	2.029	2.266	2.546
Tm	0.259	0.318	0.369
Yb	1.65	1.98	2.21
Lu	0.225	0.260	0.286

[1] BAS, basanite; [2]Replicate split of rock sample.

Strontium

Sample	Description	$^{87}Sr/^{86}Sr$ (± 2s)	$^{86}Sr/^{88}Sr$
NP-MP05-3B	Dike / WR	0.703615 ± 0.000010	0.1199
Standard			
SRM987 (600 ng)		0.710220 ± 0.000008	0.1195
SRM987 (300 ng)		0.710233 ± 0.000008	0.1200
SRM987 (600 ng)		0.710232 ± 0.000007	0.1192
NP-MP05-1	Dike / CF	0.704010 ± 0.000007	0.1191
NP-MP05-1[1]	Dike / CF	0.704025 ± 0.000007	0.1191
NP-MP05-4	Wall Rock / CF	0.704685 ± 0.000007	0.1191
NP-MP05-4[1]	Wall Rock / CF	0.704676 ± 0.000007	0.1195
Standard			
SRM987 (600ng)		0.710242 ± 0.000006	0.1198
SRM987 (600ng)		0.710245 ± 0.000007	0.1194
SRM987 (600ng)		0.710242 ± 0.000008	0.1188

[1] Duplicate analysis.

Neodynium (± 2s)

Sample	Description	$^{143}Nd/^{144}Nd$	$^{145}Nd/^{144}Nd$	$^{146}Nd/^{144}Nd$	ε_{Nd}
NP-MP05-3B	Dike / WR	0.512908 ± 0.000008	0.348403 ± 0.000005	0.7202	5.3
Standard					
La Jolla (150 ng)		0.511856 ± 0.000006	0.348411 ± 0.000005	0.7200	
La Jolla (150 ng)		0.511855 ± 0.000007	0.348407 ± 0.000004	0.7208	

Epsilon Nd calculated using modern $^{143}Nd/^{144}Nd$ for chondrite uniform reservoir (CHUR) of 0.512638.

Lead (± 2s)

Sample	Description	$^{206}Pb/^{204}Pb$	$^{207}Pb/^{204}Pb$	$^{208}Pb/^{204}Pb$
NP-MP05-3B	Dike / WR	18.3277 ± 0.0008	15.5757 ± 0.0007	38.3663 ± 0.0020
Standard				
NBS 981		16.9416 ± 0.0012	15.4995 ± 0.0011	36.7205 ± 0.0028

Carbon and Oxygen (±1s)		Yield	$\delta^{18}O$
Sample	Description	(µmoles CO_2/mg)	(‰ vs. VSMOW)
NP-MP05-1	Silicate Fraction	10.3 ± 0.2	6.5 ± 0.2
NP-MP05-1[1]	(acid leach of WR)	10.2 ± 0.2	5.8 ± 0.2

[1] Duplicate analysis.

Carbon and Oxygen (±1s)		$\delta^{13}C$	$\delta^{18}O$
Sample	Description	(‰ vs. VPDB)	(‰ vs. VSMOW)
NP-MP05-1[(a)]	Dike / CF	-4.23 ± 0.13	13.82 ± 0.09
NP-MP05-1[(a)]	Dike / CF	-4.00 ± 0.09	13.98 ± 0.10
NP-MP05-1[(a)]	Dike / CF	-3.97 ± 0.10	13.83 ± 0.07
NP-MP05-1[(b)]	Dike / CF	-3.88 ± 0.07	13.67 ± 0.05
NP-MP05-1[(b)]	Dike / CF	-3.79 ± 0.05	13.90 ± 0.06
NP-MP05-1[(c)]	Dike / CF	-4.14 ± 0.14	14.08 ± 0.14
NP-MP05-1[(d)]	Dike / CF	-3.99 ± 0.08	14.17 ± 0.14
NP-MP05-1[(d)]	Dike / CF	-3.86 ± 0.07	14.30 ± 0.10
NP-MP05-1[(e)]	Dike / CF	-4.46 ± 0.41	14.05 ± 0.47
NP-MP05-1[(e)]	Dike / CF	-4.39 ± 0.06	14.29 ± 0.07

Carbonate fractions extracted from: (a) whole rock powders; (b, c, d, e) carbonate-rich patches by powders; (b, c, d, e) carbonate-rich patches by microdrilling.

Supplementary Material SM2: $^{40}Ar/^{39}Ar$ geochronometry

Results of $^{40}Ar/^{39}Ar$ dating for the whole rock basanite dike are presented in Figure SM2. The dike is fresh and unaltered and we accept the plateau age of 18.72 ± 0.26 Ma as the sample's crystallization age (Table SM2).

Sample preparation and analysis was as follows. Samples were fed through a jaw crusher and hand-picked for clean pieces; these were crushed in a tungsten carbide ring mill and hand-picked for clean 1-2 mm diameter chips. Selected chips were washed in acetone, dried, and wrapped in aluminum foil and then stacked in an irradiation capsule with similar-aged samples and neutron flux monitors (Fish Canyon Tuff sanidine, 28.02 Ma; Renne et al., 1998). Samples were irradiated at the McMaster Nuclear Reactor in Hamilton, Ontario, for 90 MWh, with a neutron flux of approximately 4x1013 neutrons/cm2/s. Analyses (n=57) of 19 neutron flux monitor positions produced errors of <0.5 % in the J value. The samples were analyzed at the Noble Gas Laboratory of the Pacific Centre for Isotopic and Geochemical Research (PCIGR), University of British Columbia. The mineral separates were step-heated with a 10 W CO2 laser (New Wave Research™ MIR10) until fused. The gas from each step was analyzed by a VG5400 mass spectrometer equipped with an ion-counting electron multiplier. All measurements were corrected for total system blank, mass spectrometer sensitivity, mass discrimination, radioactive decay during and subsequent to irradiation, as well as interfering Ar from atmospheric contamination and the irradiation of Ca, Cl, and K (isotope production ratios: (40Ar/39Ar)K = 0.0302 ± 0.00006, (37Ar/39Ar)Ca = 1416.4 ± 0.5, (36Ar/39Ar)Ca =0.3952 ± 0.0004, Ca/K = 1.83 ± 0.01 (37ArCa/39ArK)).

XXX

Table SM2 Statistics for $^{40}Ar/^{39}Ar$ dating of sample NP-MP05-3. Error on age is 2σ.

Age (Ma)	^{39}Ar % plateau	Plateau steps	MSWD	Probability	Initial $^{40}Ar/^{36}Ar$
18.72 ± 0.26	96.2	4 to 14	0.31	0.98	297.8 ± 8.6

Ages were calculated using Isoplot 3.09 (Ludwig, 2003). Errors are quoted at the 2-sigma (95% confidence) level and propagated from all sources except mass spectrometer sensitivity and age of the flux monitor. Plateau age error includes 0.5 % J error. The best plateau and plateau age were picked based on the following criteria:

i) Three or more contiguous steps comprising more than 50 % of the 39Ar;

ii) Probability of fit of the weighted mean age greater than 5 %;

iii) Slope of error-weighted line through the plateau ages equals zero at 5 % confidence;

iv) Ages of two outermost steps on plateau do not differ from weighted-mean plateau age;

v) Outermost two steps to either side of plateau do not have nonzero slopes with same sign.

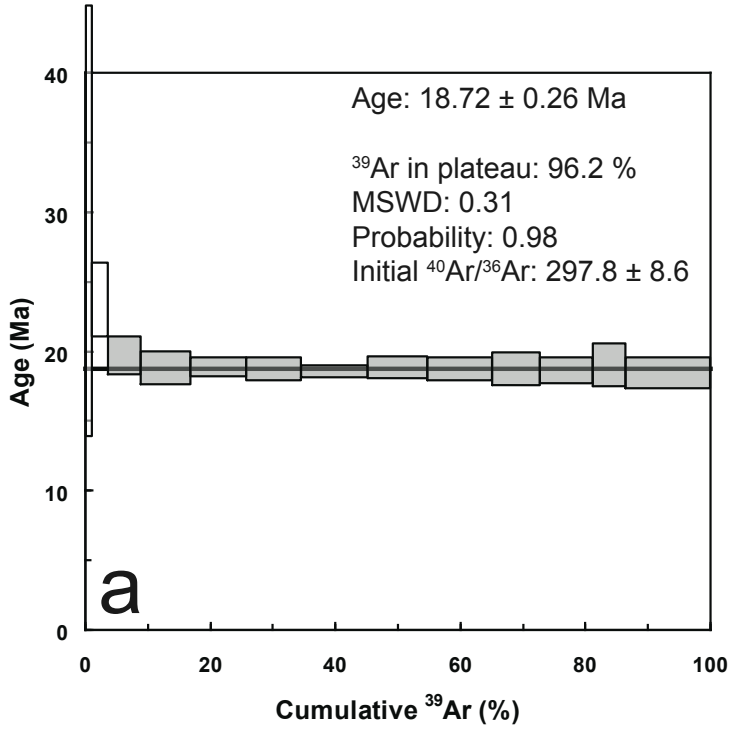

Figure SM2. Release spectra graphs for $^{40}Ar/^{39}Ar$ dating of the basanite dike (NP-MP05-3). Plateau steps are filled, rejected steps are open. Box heights and quoted errors are 2σ.

References

Jicha, B.R., Singer, B.S., & Sobol, P., 2016, Re-evaluation of the ages of 40Ar/39Ar sanidine standards and supereruptions in the western U.S. using a Noblesse multi-collector mass spectrometer: Chemical Geology, v. 431, p. 54–66, doi:10.1016/j.chemgeo.2016.03.024.

Min, K., Mundil, R., Renne, P.R., & Ludwig, K.R., 2000, A test for systematic errors in 40Ar/39Ar geochronology through comparison with U/Pb analysis of a 1.1-Ga rhyolite: Geochimica et Cosmochimica Acta, v. 64, p. 73–98, doi:10.1016/S0016-7037(99)00204-5.

Ludwig K. R. (2003) Isoplot 3.09 A Geochronological Toolkit for Microsoft Excel. BerkeleyGeochronology Center, Special Publication No. 4.

Renne P. R., Swisher, III C. C., Deino A. L., Karner D. B., Owens T. and DePaolo D. J. (1998) Intercalibration of standards, absolute ages and uncertainties in 40Ar/39Ar dating. *Chemical Geology* **145**, 117-152.

Table SM3. Major (wt. %) and trace (ppm) element compositions of Mt. Preston mantle xenoliths (MP05-).

Sample	31	31[1]	35	35[2]	44	50	69	70A	78	79A	139	159A	160A	160B	161D	162A	164A
Rock Type[3]	Lhz	Lhz	Lhz	Lhz	Lhz	Lhz	Web	Lhz	Lhz	Ol-Web	Lhz	Lhz	Lhz	Dun	Hz	Ol-Web	Lhz
SiO_2	44.21	44.24	44.11	44.26	44.29	44.61	48.07	44.40	43.53	46.12	44.38	44.45	44.60	39.83	44.06	46.54	43.95
TiO_2	0.047	0.048	0.031	0.031	0.034	0.028	0.057	0.028	0.139	0.151	0.143	0.110	0.125	0.039	0.038	0.073	0.096
Al_2O_3	2.94	2.79	2.01	1.98	2.18	2.45	11.90	2.77	3.43	6.27	4.71	2.84	4.26	0.18	1.36	5.75	2.91
Fe_2O_3	1.53	1.75	1.63	1.76	1.68	1.23	1.54	1.51	1.94	2.14	2.01	1.44	1.69	1.99	1.48	1.98	1.71
FeO	6.68	6.47	6.35	6.27	6.34	6.84	3.27	6.47	6.91	5.36	6.49	6.86	6.87	9.98	6.90	5.70	6.44
MnO	0.119	0.120	0.112	0.113	0.113	0.116	0.179	0.115	0.139	0.119	0.132	0.119	0.126	0.146	0.116	0.126	0.118
MgO	40.42	40.25	41.80	42.07	41.70	40.74	18.40	40.24	38.10	31.80	36.16	39.89	37.03	46.42	43.57	33.17	40.37
CaO	2.84	3.11	2.29	2.25	2.21	2.68	14.73	2.94	3.91	5.98	4.36	2.94	3.41	0.38	1.12	5.11	3.13
Na_2O	0.19	0.20	0.12	0.12	0.13	0.13	0.89	0.15	0.29	0.47	0.33	0.26	0.30	0.03	0.08	0.36	0.26
K_2O	0.01	0.01	0.01	0.01	0.01	<d/l	0.01	0.01	0.03	0.01	0.02	0.01	0.01	0.01	0.01	<d/l	<d/l
P_2O_5	0.017	0.017	0.017	0.017	0.017	0.016	0.017	0.016	0.031	0.021	0.024	0.023	0.025	0.026	0.018	0.017	0.019
H_2O^+	0.48	0.46	0.62	0.63	0.66	0.65	0.49	0.63	0.77	0.61	0.59	0.61	0.43	0.38	0.60	0.63	0.59
H_2O^-	0.25	0.28	0.22	0.23	0.19	0.17	0.12	0.15	0.26	0.22	0.21	0.20	0.18	0.17	0.25	0.13	0.15
CO_2	0.33	0.40	0.33	0.33	0.33	0.26	0.11	0.29	0.26	0.33	0.26	0.33	0.33	0.29	0.26	0.26	0.29
Total	99.81	99.87	99.43	99.84	99.69	99.75	99.66	99.57	99.48	99.38	99.61	99.88	99.21	99.70	99.61	99.72	99.88
LOI	0.37	0.47	0.48	0.49	0.49	0.34	0.36	0.35	0.57	0.61	0.41	0.38	0.23	<d/l	0.34	0.39	0.33
Rare Earth Elements																	
La	0.03	<d/l	0.02	0.01	0.01	0.02	0.10	0.01	0.94	0.50	0.45	0.15	0.45	0.09	0.13	0.05	0.02
Ce	0.09	0.02	0.07	0.04	0.02	0.04	0.22	0.02	1.71	0.71	0.88	0.38	0.87	0.18	0.24	0.08	0.09
Pr	0.02	<d/l	<d/l	<d/l	<d/l	<d/l	0.03	<d/l	0.21	0.09	0.12	0.07	0.12	0.02	0.03	0.01	0.03
Nd	0.07	0.03	0.04	<d/l	<d/l	<d/l	0.19	<d/l	0.96	0.49	0.62	0.41	0.63	0.10	0.14	0.12	0.26
Sm	0.04	0.04	<d/l	<d/l	<d/l	<d/l	0.12	<d/l	0.30	0.29	0.26	0.18	0.23	<d/l	0.03	0.12	0.14
Eu	0.02	0.02	<d/l	<d/l	<d/l	<d/l	0.07	<d/l	0.12	0.14	0.11	0.08	0.10	<d/l	0.01	0.07	0.06
Gd	0.12	0.13	0.05	0.04	0.05	0.04	0.57	0.07	0.52	0.67	0.49	0.31	0.39	<d/l	0.05	0.40	0.25
Tb	0.02	0.02	<d/l	<d/l	<d/l	<d/l	0.19	0.02	0.08	0.13	0.09	0.05	0.07	<d/l	<d/l	0.08	0.04
Dy	0.23	0.25	0.10	0.09	0.12	0.13	2.24	0.19	0.62	1.03	0.68	0.40	0.55	<d/l	0.06	0.76	0.33
Ho	0.06	0.06	0.03	0.03	0.03	0.03	0.73	0.05	0.13	0.23	0.15	0.09	0.12	<d/l	0.01	0.19	0.07
Er	0.18	0.21	0.09	0.09	0.11	0.12	2.84	0.17	0.38	0.72	0.46	0.27	0.37	<d/l	0.04	0.61	0.22
Tm	0.03	0.03	0.02	0.02	0.02	0.02	0.52	0.03	0.06	0.11	0.07	0.04	0.06	<d/l	0.01	0.10	0.03
Yb	0.20	0.22	0.12	0.11	0.13	0.15	3.64	0.21	0.37	0.69	0.43	0.26	0.35	<d/l	0.05	0.62	0.21
Lu	0.04	0.04	0.02	0.02	0.02	0.03	0.64	0.04	0.06	0.11	0.07	0.04	0.06	<d/l	<d/l	0.10	0.04

[1]Duplicate analysis. [2]Replicate sample from rock splitting. [3]Lhz, lherzolite; Web, websterite; Hz, Harzburgite; Dun, Dunite.

Table SM4. Geothermometry results (°C) for mantle xenoliths based on Brey and Köhler (1990) with sample density (ρ; g cm^{-3}) and carbonate textures (G, grains; V, veins). All sample numbers prefixed by MP05.

Sample	Density	T_{ave}	1σ	T_{max}	T_{min}	Textures
A1	3.314 ± 0.015	911	5	917	903	V
A2	3.306 ± 0.007	834	17	855	805	V
A4	3.311 ± 0.010	912	19	943	891	V
31	3.300 ± 0.012	876	5	883	870	G/V
32	3.285 ± 0.009	843	18	862	809	G/V
33	3.307 ± 0.003	876	10	888	865	V
34A	3.320 ± 0.024	924	14	942	912	V
34B	3.309 ± 0.013	883	17	903	862	V
35	3.289 ± 0.007	888	13	907	877	G/V
44	3.296 ± 0.038	888	9	898	873	V
45	3.309 ± 0.014	901	13	917	886	G
50	3.292 ± 0.013	849	21	869	809	G/V
56A	3.313 ± 0.011	944	7	952	936	G/V
69	3.281 ± 0.004	850	17	870	823	G
70A	3.300 ± 0.009	889	9	902	878	G/V
72	3.302 ± 0.006	908	15	928	890	G/V
74	3.279 ± 0.019	914	14	929	891	G/V
78	3.302 ± 0.018	931	10	941	917	G/V
79A	3.282 ± 0.004	935	10	954	925	G/V
81A	3.293 ± 0.008	917	6	925	911	G/V
85	3.283 ± 0.017	901	17	924	887	G/V
89	3.274 ± 0.006	899	17	918	877	G/V
90	3.312 ± 0.012	881	15	905	859	G/V
95	3.298 ± 0.010	873	21	899	849	G/V
96	3.299 ± 0.011	874	12	884	851	G
101	-	901	15	922	878	G/V
110	3.316 ± 0.014	901	17	925	881	G/V
113	3.314 ± 0.014	896	14	913	877	G/V
118	-	918	8	930	906	G/V
121A	3.303 ± 0.004	913	18	926	887	G/V
121B	3.296 ± 0.008	880	25	908	850	G/V
139	3.300 ± 0.011	901	7	913	895	G/V
149	3.332 ± 0.012	815	18	831	792	G/V
156A	3.302 ± 0.007	940	14	955	914	G/V
157A	-	929	16	952	913	G/V
157B	3.293 ± 0.007	896	14	909	878	G/V
159A	3.304 ± 0.012	931	11	950	917	V
160A	3.310 ± 0.041	979	9	987	962	G/V
160B	3.350 ± 0.005	1119	5	1126	1112	G/V
161A	3.297 ± 0.012	932	9	942	917	G/V
161B	3.365 ± 0.006	892	24	912	858	G
161D	3.290 ± 0.008	851	19	879	821	G/V
162A	3.309 ± 0.034	897	9	908	887	G/V
163A	3.280 ± 0.013	892	14	909	870	G/V
163C	3.284 ± 0.011	894	18	915	872	G/V
164A	3.302 ± 0.020	894	8	903	886	G/V
164B	3.297 ± 0.003	826	23	869	807	V
164C	3.266 ± 0.020	845	15	868	828	G/V
165A	3.312 ± 0.004	951	22	978	922	G/V
166	3.308 ± 0.005	932	11	948	915	G/V
Min	3266	815		831	792	
Max	3365	1119		1126	1112	